Autophagy-mediated NCOR1 degradation is required for brown fat maturation and thermogenesis

Alba Sabaté-Pérez[1,2,3], Montserrat Romero[1,2,3], Paula Sànchez-Fernàndez-de-Landa[1,2,3], Stefania Carobbio[4,5], Michail Mouratidis[1], David Sala[1,2,3], Pablo Engel[6], Josep A Villena [3,7], Sam Virtue[4], Antonio Vidal-Puig[4,8], Manuel Palacín[1,2,9], Xavier Testar[2,3], and Antonio Zorzano[1,2,3]*

[1]Institute for Research in Biomedicine (IRB Barcelona). The Barcelona Institute of Science and Technology, Barcelona, Spain.

[2]Departament de Bioquímica i Biomedicina Molecular, Facultat de Biologia, Universitat de Barcelona, 08028 Barcelona, Spain.

[3]CIBER de Diabetes y Enfermedades Metabólicas Asociadas (CIBERDEM), Instituto de Salud Carlos III, Spain.

[4]Metabolic Research Laboratories, Institute of Metabolic Science, Addenbrooke's Hospital, University of Cambridge, Cambridge, CB2 0QQ, UK.

[5]Centro de Investigacion Principe Felipe, Valencia, Spain.

[6]Immunology Unit, Department of Biomedical Sciences, Faculty of Medicine and Health Sciences, Universitat de Barcelona, Spain.

[7]Laboratory of Metabolism and Obesity, Vall d'Hebron-Institut de Recerca, Universitat Autònoma de Barcelona, 08035 Barcelona, Spain.

[8]Wellcome Trust Sanger Institute, Wellcome Trust Genome Campus, Hinxton, Cambridge, CB10 1SA, UK.

[9]CIBER de Enfermedades Raras (CIBERER), Instituto de Salud Carlos III, Spain.

*Corresponding author. Institute for Research in Biomedicine, C/ Baldiri Reixac 10, 08028 Barcelona. Tel:+34-934037197; Fax:+34-934034717; E-mail: antonio.zorzano@irbbarcelona.org

Abstract

Brown adipose tissue (BAT) thermogenesis affects energy balance, and thereby it has the potential to induce weight loss and to prevent obesity. Here we document a macroautophagic/autophagic-dependent mechanism of PPARG activity regulation that induces brown adipose differentiation and thermogenesis, and that is mediated by TP53INP2. Disruption of TP53INP2-dependent autophagy reduced brown adipogenesis in cultured cells. *In vivo* specific-*tp53inp2* ablation in brown precursor cells or in adult mice decreased the expression of thermogenic and mature adipocytes genes in BAT. As a result, TP53INP2-deficient mice had reduced UCP1 content in BAT and impaired maximal thermogenic capacity, leading to lipid accumulation and to positive energy balance. Mechanistically, TP53INP2 stimulates PPARG activity and adipogenesis in brown adipose cells by promoting the autophagic degradation of NCOR1, a PPARG co-repressor. Moreover, the modulation of TP53INP2 expression in BAT and in human brown adipocytes suggest that this protein increases PPARG activity during metabolic activation of brown fat. In all, we have identified a novel molecular explanation to the contribution of autophagy to BAT energy metabolism that could facilitate the design of therapeutic strategies against obesity and its metabolic complications.

Keywords

Autophagy; brown adipose tissue; metabolism; obesity; thermogenesis

Abbreviations

BAT: brown adipose tissue; GTT: glucose tolerance test; HFD: high fat diet; ITT: insulin tolerance test; MAP1LC3/LC3: microtubule-associated protein 1 light chain 3; NCOR1: nuclear receptor co-repressor 1; PPARG/PPARγ: peroxisome proliferator-activated receptor gamma; TRP53INP2/TP53INP2: transformation related protein 53 inducible nuclear protein 2; UCP1: uncoupling protein 1 (mitochondrial, proton carrier); WAT: white adipose tissue.

Introduction

Brown adipose tissue (BAT) uses nutrients to produce heat in order to maintain body temperature through non-shivering adaptive thermogenesis, and plays a relevant role in energy expenditure [1, 2]. Brown adipocytes contain many lipid droplets and mitochondria that express UCP1 (uncoupling protein 1 (mitochondrial, proton carrier)), the final effector of heat dissipation. Functional BAT depots have been detected in lean adult humans that can be activated by cold exposure [3-5]. Of relevance, human BAT activity correlates with lower body mass index (BMI) and improved glycemia [3, 6], and associates with cardiometabolic health [7] indicating that strategies that could increase BAT mass and/or its activation could become promising targets to combat obesity and its metabolic complications.

Macroautophagy/autophagy has been reported to modulate the differentiation and the metabolic activity of BAT. Initial studies showed that concurrent depletion of the autophagic protein ATG7 in white and brown adipocytes promoted a decrease in the mass of interscapular BAT, as well as lower deposition of lipid droplets, consequence of increased beta-oxidation [8]. Later, the selective depletion of ATG7 in $MYF5^{+}$ (myogenic factor 5) progenitors (including brown preadipocytes) showed that autophagy is required for BAT differentiation and function. Thus, BAT from MYF5-specific *atg7* KO mice had diminished levels of UCP1 and mitochondrial markers, which limited its thermogenic capacity and resulted in the enlargement of its lipid droplets [9]. The contribution of autophagy receptor proteins such as SQSTM1/p62 or NBR1 in brown adipocytes has also been evaluated, which revealed that actually they affect thermogenesis through non-autophagic dependent mechanisms, but rather through the modulation of nuclear functions [10, 11]. Specifically, SQSTM1 has been reported to activate the transcription factor ATF2 [12], and to promote the formation of PPARG/PPARγ (peroxisome

proliferator-activated receptor gamma)-RXR (retinoid X receptor) heterodimers, whereas NBR1 inhibits PPARG-RXR association in brown adipocytes [11]. These observations are relevant since PPARG is an essential transcription factor in brown adipogenesis [13-15], and genetic mutations that impair its activity are associated with decreased BAT development and thermogenic capacity [16]. Yet, the reasons why autophagy activity per se is essential for brown adipogenesis and thermogenesis remain to be elucidated.

In this work, we have focused on the modulator protein TRP53INP2/TP53INP2 (for the mouse or human transformation related protein 53 inducible nuclear protein 2 respectively, and thereafter referred as TP53INP2 for both proteins for simplicity), which induces autophagy in different *in vitro* models and also in mice [17-19]. We provide evidence supporting the concept that TP53INP2-dependent autophagy promotes brown adipose maturation and maintains the metabolic properties of brown adipocytes. Mechanistically, TP53INP2 sustains PPARG activity and brown fat differentiation through the autophagy-mediated degradation of NCOR1 (nuclear receptor co-repressor 1) in brown adipose cells.

Results

Autophagy is required for the differentiation and maturation of brown adipocytes.

Initially, we analyzed the role of autophagy on the capacity of brown preadipocytes to undergo differentiation into adipocytes. To this end, we focused into the autophagy protein TP53INP2, which accelerates autophagy in different cell types, and its loss-of function *in vitro* and *in vivo* reduces but does not cancel autophagy flux [17, 19-21]. Brown preadipocytes were isolated from *Tp53inp2 LoxP*$^{+/+}$ mice and they were immortalized. The *tp53inp2* ablation (KO) was conducted by adenoviral-mediated Cre-recombinase expression. *Tp53inp2* mRNA and protein expression was undetectable in KO cells compared to controls (Figures S1A and S1B). In keeping with the autophagy function of TP53INP2 documented in other cell types [17, 19, 20], autophagy flux, measured by the accumulation of MAP1LC3/LC3B-II upon bafilomycin A_1 treatment, was markedly impaired in *tp53inp2* KO preadipocytes (Figures 1A and 1B). To further validate these results, we also measured autophagy flux in brown preadipocytes upon acute repression of TP53INP2 induced by siRNA transfection. LC3B-II accumulation upon bafilomycin A_1 was reduced when using *Tp53inp2* siRNA compared to siScramble (siSCR) transfected cells (Figures 1C and 1D). Importantly, the repression of TP53INP2 also reduced its autophagic degradation as detected by a low accumulation upon autophagy inhibition (Figures 1C and S1C). This suggests that TP53INP2 is also degraded through autophagy, and that this process is altered when the protein is downregulated.

Once validated the autophagic function of TP53INP2 in brown preadipocytes, these cells were induced to differentiate for 9 days, as reported [22]. Morphological analysis of differentiated brown adipocytes revealed that KO preadipocytes lost their adipogenic

capacity compared to respective control cells (Figure 1E). Protein expression analysis showed that KO preadipocytes presented reduced PPARG1 and PPARG2 induction in response to differentiation (Figures 1F, S1D and S1E). Moreover, mitochondrial biogenesis, assessed by the increase in mitochondrial proteins TIMM44 and MFN2, and the thermogenic protein UCP1, was blunted in *tp53inp2* KO adipocytes (Figures 1F, S1F-H). KO adipocytes also exhibited downregulation of genes involved in brown adipogenesis, such as *Prdm16* and *Pparg1*, and reduced mRNA levels of genes encoding mitochondrial proteins, such as *Ucp1*, *Cox7a1* and *Cox8b* (Figure 1G). In parallel studies, *tp53inp2* downregulation (KD) was induced by lentiviral *Tp53inp2* siRNA stable expression, which achieved a 70% repression (Figures S1I and S1J). *tp53inp2* KD cells also showed impaired adipogenic potential and reduced expression of protein markers (Figures S1K-M). In order to provide an independent evidence for a role of autophagy on brown adipogenesis, we differentiated brown preadipocytes with a submaximal concentration of chloroquine during different times. Chloroquine treatment for the last 3 or 7 days of the differentiation protocol induced a time-dependent accumulation of LC3B-II (Figure 1H and S1N), along with reduced expression of adipogenic markers PPARG2, PPARG1 and UCP1 (Figure 1H and S1O-Q). These results further support a role of autophagy in brown adipocyte differentiation.

As we found that TP53INP2 is required for brown adipocyte differentiation, we next assessed whether this process is involved in the acquisition of metabolic properties of BAT. With that aim, we generated a *Myf5*-specific *tp53inp2* KO (KO^{Myf5}) mice by crossing *Tp53inp2 LoxP*$^{+/+}$ mice with Cre-recombinase-expressing animals under the control of the BAT and skeletal muscle precursor cell-specific promoter *Myf5* [23]. We selected this specific ablation because our interest was to determine the role of TP53INP2 on brown differentiation *in vivo*, and we had previously reported that the specific *tp53inp2*

149 ablation in muscle does not alter body weight, adiposity, glucose metabolism or
150 mitochondrial content and functionality in muscle [19]. Gene expression analysis showed
151 that *Tp53inp2* mRNA levels were specifically reduced in iBAT and muscle (Figure S2A),
152 and unchanged compared with control (LoxP) littermates in all other tissues evaluated. In
153 addition, TP53INP2 protein levels were also ablated in BAT from KO^{Myf5} mice (Figure
154 S2B). The resulting KO^{Myf5} mice were born in normal Mendelian ratios and were
155 indistinguishable from their LoxP littermates. At 3 months of age, no changes were found
156 in body weight, composition or tissue weight in either male or female *tp53inp2* KO mice
157 (Figures S2C-G). However, iBAT weight was significantly increased in male KO^{Myf5}
158 mice (Figure 1I), thereby suggesting an early alteration in this tissue. Histological
159 examination of iBAT showed a loss of multilocularity in *tp53inp2* KO iBAT compared
160 to controls in both sexes (Figures 1J and S2H), characterized by a marked reduction in
161 lipid droplet (LD) number per area unit and an increase in LD size (Figures S2I and S2J).
162 These morphological alterations are associated to thermogenically incompetent BAT [24-
163 26]. In contrast, two major white adipose depots, namely inguinal WAT (ingWAT) and
164 perigonadal WAT (pgWAT), showed similar weights in both sexes and genotypes
165 (Figures S2K and S2L). The fact that KO^{Myf5} mice do not show reduced brown fat mass
166 indicates that TP53INP2 is dispensable for embryonic brown adipose development, or
167 that its function *in vivo* is compensated by other factors. To further characterize the
168 alterations occurring in BAT we analyzed total DNA in the whole iBAT depot and we
169 also performed histological analyses. Total DNA per iBAT depot was unchanged between
170 genotypes (Figure S2M), indicating that the total number of cells was not altered upon
171 TP53INP2 depletion. Additional histological analyses using wheat germ agglutinin
172 (WGA, to label the cell surface), DAPI (to label the nuclei) and anti-UCP1 antibody (to
173 measure the differentiation state of brown adipocytes) were performed in iBAT sections.

Triple staining showed a reduced abundance of UCP1 in brown adipocytes from KO^{Myf5} mice, again validating a reduced adipose differentiation (Figure 1K and S2N). In addition, data showed an altered cell size distribution of adipocytes in KO^{Myf5} mice, with a greater abundance of larger adipocytes and with less smaller cells (Figure S2O), which occurred in the absence of changes in the number of nuclei or in the number of adipocytes per surface unit (Figures 1K, S2P and S2Q). These data clearly indicate the existence of hypertrophy of brown adipocytes in BAT from KO^{Myf5} mice. In all, these evidences also indicate that TP53INP2 probably functions in brown adipose maturation or in brown adipocyte cell fate maintenance in adult mice, thus its ablation reduces BAT thermogenic capability leading to lipid accumulation and brown adipocyte enlargement.

To test this hypothesis, we evaluated the expression of adipogenic and thermogenic genes in iBAT. The results revealed a reduced expression of the adipogenic genes *Prdm16*, *Cebpb*, *Pparg1* and *Pparg2* in *tp53inp2* KO iBAT, as well as of that involved in BAT thermogenesis, such as *Ucp1*, *Ppargc1a/Pgc1α*, *Cox8b*, *Cox7a1*, *Dio2* and *Elovl3* (Figure 1L). The mRNA levels of the *Dlk1*/*Pref1* (delta like non-canonical Notch ligand 1), known to inhibit adipogenesis in preadipocytes, was also significantly enhanced in KO^{Myf5} mice compared to control animals (Figure S2R). Taken together, our data indicate that TP53INP2 is required for the proper metabolic maturation of brown adipocytes *in vivo*.

TP53INP2-dependent autophagy is also required for the maintenance of the differentiation state of brown adipocytes.

Next, we evaluated whether TP53INP2-dependent autophagy, in addition to regulating brown adipose differentiation, also maintains the maturation state of brown adipocytes.

198 To do so, we treated *in vitro* differentiated brown adipocytes isolated from Cre-
199 recombinase-inducible *Tp53inp2 LoxP*$^{+/+}$ mice with tamoxifen for 3 days, to induce
200 TP53INP2 repression. Tamoxifen treatment efficiently reduced *Tp53inp2* mRNA levels
201 by 60%, but also significantly downregulated the expression of *Prdm16*, *Ucp1* and
202 *Ppargc1a*, which are brown adipogenic and thermogenic genes, compared to vehicle
203 (DMSO)-treated adipocytes (Figure 2A). Under these conditions, the expression of
204 *Cox7a1*, *Cox8b* or *Pparg2* was unchanged (Figure 2A). No difference in gene expression
205 was found when using *in vitro* differentiated brown adipocytes without Cre-recombinase
206 expression under the same experimental conditions (Figure 2B). To determine the role of
207 TP53INP2 in mature brown adipocytes *in vivo*, we eliminated it from adult mice by
208 tamoxifen administration to Cre-recombinase-inducible *Tp53inp2 LoxP*$^{+/+}$ mice [20]
209 under the control of the *Ubc* (ubiquitin C) promoter. A tamoxifen diet was administered
210 to both Cre-positive (KO^{Ubc}) and Cre-negative (LoxP) mice for one month, leading to
211 TP53INP2 loss-of-function in iBAT (Figures S3A and S3B). Six months after the onset
212 of tamoxifen treatment, KO^{Ubc} mice showed an increased iBAT weight compared with
213 control littermates (Figure 2C). Under these conditions, body weight was also enhanced
214 in KO^{Ubc} mice (Figure S3C), in keeping with reported data [20]. Under these conditions,
215 all adipose depots analyzed in KO^{Ubc} mice were enhanced (ingWAT and pgWAT), liver
216 weight was also increased, and no changes were detected in quadriceps, gastrocnemius
217 and tibialis anterior muscles (Figures 2C and S3D). Histological staining of iBAT
218 sections again revealed a thermogenically inactive morphology (Figure 2D), as reflected
219 by an increase in LD size and a decrease in LD number per surface (Figures 2E and 2F).
220 Moreover, the number of adipocytes or nuclei per surface unit and UCP1 protein
221 abundance was decreased in KO^{Ubc} mice (Figures 2G, 2H, S3E and S3F), and adipocyte
222 area was enhanced (Figure 2I). Gene expression analysis of iBAT samples showed that

223 KO^{Ubc} mice had a similar expression profile to that of KO^{Myf5} mice, characterized by
224 reduced expression of BAT adipogenic genes, including *Pparg2* and *Cebpb,* accompanied
225 by downregulation in genes related to thermogenesis (Figure 2J). Altogether, our data
226 indicate that TP53INP2 plays a key role in the maintenance of the differentiation state of
227 mature brown adipocytes under *in vivo* conditions.

228

229 ***TP53INP2 induces BAT PPARG activity.***

230 As we found that TP53INP2-dependent autophagy is required for brown adipocyte
231 differentiation and for the maintenance of mature BAT properties, we next analyzed the
232 mechanisms involved. To this end, we performed microarray gene expression profiling
233 using iBAT samples from KO^{Myf5} and from LoxP mice as controls. More than 700 genes
234 were significantly upregulated and 464 were downregulated by *tp53inp2* ablation (Figure
235 3A). In addition, to examine the impact of TP53INP2 downregulation on BAT gene
236 modulation, we compared our microarray results with published RNAseq data evaluating
237 the transcriptomic changes associated to thermoneutrality [27]. In this study, the authors
238 compared gene expression from iBAT samples of mice housed at 30°C with mice housed
239 under standard conditions (22°C). Interestingly, around 40% of the genes modulated by
240 the lack of TP53INP2 in iBAT were also naturally modified by the physiological
241 inhibition of thermogenesis (Figure 3A). Moreover, we defined two gene sets with the
242 top 100 up- and top 100 downregulated genes by *tp53inp2* ablation in iBAT, and analyzed
243 them in the 22°C vs 30°C RNAseq. Our results showed that the top hits in the
244 KO^{Myf5}/LoxP experiment were over-represented in the extremes of the 30°C/22°C ranked
245 list, being modulated with a common direction (Figures 3B and 3C), which indicates that

246 the gene variation showed a similar pattern in both conditions (thermoneutrality and
247 *tp53inp2* ablation).

248 The transcriptomic profiling of iBAT samples from KO^{Ubc} and from LoxP mice also
249 identified a substantial number of dysregulated genes (291 genes were upregulated and
250 250 genes were downregulated) by *tp53inp2* ablation. Gene set enrichment analysis
251 revealed several dysregulated pathways upon *tp53inp2* ablation, both in KO^{Myf5} (Figure
252 3D) and in KO^{Ubc} mice (Figure 3E). Importantly, one of the most significantly
253 downregulated gene sets by the absence of TP53INP2 in the two mouse models was
254 adipogenesis (Figures 3D, 3E and S4A), further validating the view that TP53INP2
255 induces brown fat differentiation. Fatty acid metabolism, oxidative phosphorylation and
256 peroxisome gene sets were also downregulated in both mouse models (Figures 3D, 3E,
257 S4B and S4C), revealing that BAT oxidative metabolism is compromised when
258 TP53INP2 is depleted. These data indicate the existence of common defective processes
259 operating in BAT from KO^{Myf5} and from KO^{Ubc} mice upon *tp53inp2* ablation.

260 Further exploration of additional gene sets affected revealed a significant downregulation
261 of the PPAR signaling pathway upon loss of TP53INP2 in BAT in KO^{Myf5} mice (Figure
262 3F), and in KO^{Ubc} mice (Figure S4D). These findings are of interest since it has been
263 documented that TP53INP2 overexpression co-regulates the transcriptional activity of
264 various nuclear receptors, including PPARs [21], and, in addition, PPARG is an essential
265 protein for brown adipogenesis [13-15]. Thus, we next focused on the potential role of
266 TP53INP2 in the modulation of PPAR transcriptional activity in the context of mouse
267 brown preadipocytes. PPAR response element (PPRE) transcriptional activity was
268 measured upon the addition of rosiglitazone, a PPARG-specific ligand. Preadipocytes
269 displayed low PPARG activity even in the presence of rosiglitazone, consistent with a
270 low endogenous expression of PPARG protein (Figure 3G). Thus, scramble and *tp53inp2*

KD cells were co-transfected with PPARG and treated with vehicle (-) or with rosiglitazone (+) to enhance PPRE activity. Under these conditions, *tp53inp2* KD cells showed a reduced response, thereby implying a disruption in PPAR transcriptional activity (Figure 3G). *tp53inp2* KO preadipocytes also displayed a similar profile of changes (Figure S4E). In addition, control and *tp53inp2* KO preadipocytes stably expressing PPARG (+) or empty vector (-) were incubated in the presence or absence of rosiglitazone. Ligand-induced PPARG transcriptional activity was completely blunted in TP53INP2-deficient cells stably expressing HA-PPARG (Figure 3H). Taken together, our evidence indicates that the lack of TP53INP2 in brown preadipocytes results in defective PPARG activity, which is independent of PPARG protein levels.

TP53INP2-dependent autophagy promotes the degradation of the co-repressor NCOR1.

The presence of co-repressors and co-activators modulates PPARG activity. Under inactive conditions, PPARG is physically bound to a co-repressor complex containing NCOR1. However, when PPARG binds to its ligand, a conformational change results in the release of the co-repressor complex and the binding with the co-activator complex [28]. NCOR1 has recently reported to be a substrate of autophagy [29, 30], and TP53INP2 participates in this process [17, 19]. Thus, we analyzed whether TP53INP2 regulates NCOR1 through this degradative pathway. TP53INP2-deficient brown preadipocytes showed a marked upregulation of NCOR1 protein levels under basal conditions (Figure 4A), which is in concordance with a reduced PPARG activity as documented. We also analyzed the rate of degradation of NCOR1 through the autophagy pathway. To this end, control and *tp53inp2* KD cells were incubated in the absence or presence of bafilomycin

295 A_1, and we measured the build-up of autophagy markers and NCOR1. Results revealed
296 that TP53INP2-deficient cells exhibited reduced autophagy flux and decreased
297 autophagic degradation of NCOR1 (Figures 4A-C). Alterations in NCOR1 protein
298 abundance were not associated to changes in mRNA levels (Figure S5A). Acute
299 repression of *Tp53inp2* mediated by siRNA transfection also reduced autophagic
300 degradation of NCOR1 (Figures S5B and S5C). As TP53INP2 overexpression has been
301 reported to enhance autophagy activity [17], we tested whether it could also mediate
302 enhanced NCOR1 degradation through this pathway. Thus, TP53INP2 stable
303 overexpressing brown preadipocytes were generated. Coherent with reported data[17],
304 TP53INP2 overexpression enhanced LC3B-II accumulation upon bacilomycin A_1
305 treatment, and also increased autophagic degradation of NCOR1 in brown preadipocytes
306 (Figures 4D-F). However, overexpression of a form of TP53INP2 with a mutation on its
307 LIR motif (TP53INP2-LIR) that lacks its capacity to interact with Atg8-family proteins
308 and to induce autophagy, did not alter LC3B-II or NCOR1 autophagy fluxes (Figures 4D-
309 F). TP53INP2-LIR expression was higher than TP53INP2 WT (Figure S5D), which may
310 be a consequence of a reduced degradation through autophagy (Figure S5E).

311 Next, we studied whether TP53INP2 also mediates NCOR1 degradation during
312 differentiation of brown preadipocytes. PPARG expression is highly induced from day 2
313 to 4 of differentiation (Figures S1D and S1E). Thus, we reasoned that under these
314 conditions, autophagic degradation of NCOR1 should increase in order to propitiate
315 PPARG activation. With that idea in mind, we induced TP53INP2 downregulation from
316 day 2 to 4 of differentiation by siRNA transfection, and then evaluated autophagy flux at
317 day 4. TP53INP2 repression reduced LC3B-II autophagic flux and also TP53INP2
318 degradation through autophagy (Figures 4G, S5F and S5G), similarly to preadipocytes
319 (Figures 4A-C, S5B and S5C). Importantly, NCOR1 levels in si*Tp53inp2* adipocytes were

also increased compared to siSCR cells, and its degradation rate through autophagy was lower (Figures 4G and S5H). Enhanced NCOR1 protein abundance was also detected in iBAT from KO^{Myf5} compared to LoxP mice (Figures 4H and 4I), supporting the idea that TP53INP2-mediated autophagic degradation of NCOR1 also occurs *in vivo*.

Considering that autophagy-mediated NCOR1 degradation occurs in the cytosol upon translocation of the co-repressor from the nucleus [29, 30] and that TP53INP2 recycles between nucleus and cytosol [31], we analyzed the subcellular distribution of NCOR1 by imaging and by subcellular fractionation. Coherent with its co-repressor function, NCOR1 mainly localized in the nucleus (Figures 5A and 5B). However, confocal microscopy showed that TP53INP2-deficient preadipocytes displayed greater levels of nuclear NCOR1 (Figures 5A and 5B). Enhanced abundance of NCOR1 was also detected in nuclear fractions from *tp53inp2* KD preadipocytes (Figures 5C and 5D). In contrast, TP53INP2 overexpression reduced the localization of NCOR1 in the nuclei, an effect that was not induced by TP53INP2-LIR (Figures S5I-M). These data support the view that the autophagic activity of TP53INP2 is instrumental for the proper cytosolic shuttling of NCOR1 and its regulation by autophagy, thus, TP53INP2 repression impedes NCOR1 cytosolic transport and in turn, its degradation.

Next, we analyzed whether the function of TP53INP2 on NCOR1 involves the formation of a complex between the two proteins. With that aim, we investigated whether TP53INP2 interacts with NCOR1 in HEK cells stably expressing empty vector (-) or HA-TP53INP2 (+). The affinity isolation of HA-tagged TP53INP2 protein with anti-HA beads revealed co-immunoprecipitation of endogenous NCOR1 (Figure 5E). Furthermore, the endogenous immunoprecipitation with an anti-NCOR1 antibody in HEK cells specifically detected NCOR1 protein, which co-immunoprecipitated with HA-TP53INP2 (Figure 5F). We also validated the interaction of NCOR1 with TP53INP2 in brown

preadipocytes by proximity ligation assays (PLA) (Figures 5G and 5H). Moreover, we detected that the interaction of the two proteins was maintained by TP53INP2-LIR (Figures 5G and 5H). These data suggest that NCOR1 and TP53INP2 participate in a complex, and that TP53INP2 could facilitate the translocation of NCOR1 to the cytosol for its autophagic degradation.

To evaluate if the decreased PPARG activity detected in TP53INP2-deficient preadipocytes is a consequence of increased NCOR1 abundance, we repressed NCOR1 in control and TP53INP2-deficient cells, and monitored PPARG activity. Interestingly, the downregulation of the co-repressor NCOR1 rescued the transcriptional defect observed in *tp53inp2* KD cells (Figure 5I). In the absence of PPARG ligand, NCOR1 knockdown significantly stimulated PPRE activity both in SCR and in *tp53inp2* KD compared with siCtr transfected cells (Figure 5I). In contrast, in the presence of rosiglitazone, which induces PPARG activity, the increase in PPARG transcriptional activity induced by the downregulation of NCOR1 was only significant in *tp53inp2* KD cells (Figure 5I) demonstrating that NCOR1 exerts stronger PPARG repression when TP53INP2 is deficient.

Overall, our data indicate that TP53INP2 activates the autophagic degradation of NCOR1 in brown adipose cells, through a process that involves the formation of a complex and the movement of NCOR1 from the nucleus to the cytosol. This leads to the activation of PPARG, which in turn promotes the normal induction of brown adipogenesis.

Loss of BAT-specific TP53INP2 results in thermogenic dysfunction and altered energy balance.

Based on the processes triggered by TP53INP2-dependent autophagy we next addressed the metabolic implications induced by the lack of TP53INP2 in BAT. Indirect calorimetry assays revealed that KO^{Myf5} mice significantly reduced O_2 consumption, CO_2 production and energy expenditure (Figures 6A-C and S6A-C). The decrease in energy expenditure was detected mainly in the light phase, pointing to a thermogenic defect (Figure S6D). These alterations were observed in the absence of changes in locomotor activity (Figure S6E) or in food and water intake (Figures S6F and S6G). The respiratory exchange ratio (RER) and nutrient oxidation were unchanged in KO^{Myf5} mice (Figures S6H-J). To determine whether the decreased energy expenditure was indeed a defect in BAT-specific non-shivering thermogenesis, calculated as the differential increase in oxygen consumption caused in response to adrenergic stimuli when analyzed under different thermogenic conditions [32], we measured whole body norepinephrine (NE)-induced VO_2 (ΔVO_2) in anesthetized mice housed at a range of temperatures. Under low thermogenic conditions (30°C), both LoxP and KO^{Myf5} mice showed a similar capacity to induce oxygen consumption in response to NE (Figures 6D and 6E). However, when mice were housed under standard conditions (22°C), which induces significant BAT thermogenic activity, KO^{Myf5} mice presented blunted NE-induced VO_2 compared with control littermates (Figures 6D and 6E). Our results demonstrate a defective maximal thermogenic capacity caused by the loss of TP53INP2 (Figures 6D and 6E). To further confirm that BAT dysfunction contributed to the decrease in whole-body energy expenditure, we directly measured mitochondrial respiration using high-resolution respirometry. Indeed, mitochondrial complex II activity decreased in iBAT mitochondrial-enriched fractions from KO^{Myf5} mice (Figure 6F). Under these conditions, no alterations in mitochondrial respiration were detected in tibialis anterior muscles (Figure S6K). Furthermore, the skeletal muscle-specific *tp53inp2* knockout mice

393 (KO^{Mlc1}) displayed normal metabolic parameters, showing similar energy expenditure,
394 locomotor activity and substrate utilization than control mice (Figures S6L-R), supporting
395 the view that the metabolic defects documented in KO^{Myf5} mice are associated with a
396 deficient BAT thermogenesis. In addition to these findings, cultured *tp53inp2* KO brown
397 adipocytes showed a reduced capacity to induce *Ucp1* or *Prdm16* in response to the β3-
398 adrenergic agonist CL-316,243 (CL) (Figures S6S and S6T), and a blunted ability to
399 increase oxygen consumption when treated with NE *in vitro* (Figure S6U), proving that
400 the metabolic alterations are cell autonomous.

401 The energy imbalance observed in 3-month-old *tp53inp2* KO mice occurred in the
402 presence of unaltered body weight, and with a non-significant trend for an increased fat
403 mass. Based on this, we analyzed the gain of body weight and of fat mass in a group of
404 mice studied at either 3 or 6 months, which were maintained at 22°C and subjected to a
405 control chow diet. Data clearly indicated that at 6 months of age, male KO^{Myf5} mice were
406 heavier, had more fat mass than controls, and similar lean mass (Figures 6G, S7A and
407 S7B). iBAT from male KO^{Myf5} mice weighed twice as much as that of LoxP animals
408 (Figure 6H). Expansion of both the ingWAT and the pgWAT depots was markedly more
409 significant in *tp53inp2* KO mice (Figures S7C and S7D). As a result, male KO^{Myf5} mice
410 showed a greater body weight gain and fat mass gain between 3 and 6 months of age
411 (Figures 6I and 6J). Our data clearly indicate that the reduced BAT metabolism of
412 TP53INP2 depleted mice leads to energy imbalance and greater fat mass gain.

413 Histological analysis of iBAT confirmed that tissue morphology was severely impaired
414 and the loss in multilocularity caused by *tp53inp2* ablation was exacerbated at 6 months
415 compared to 3 months both in male and in female mice (Figures S7E-G). Again, brown
416 adipocytes from KO^{Myf5} displayed hypertrophy, monitored by an increased adipocyte area
417 (Figures 6K and S7H), and by reduced number of nuclei or adipocytes per surface

418 (Figures S7I and S7J). Coherent with the decreased maximal thermogenic capacity
419 documented in KO^{Myf5}, iBAT displayed a marked reduction in UCP1 protein expression
420 (Figures 6K, 6L, S7K and S7L).

421 In addition to the disruption of BAT metabolism, KO^{Myf5} mice showed systemic
422 alterations. Thus, both males and females KO^{Myf5} mice showed impaired glucose use in
423 glucose tolerance test (GTT) assays (Figures S7M and S7N), which occurred in the
424 presence of fasting hyperinsulinemia in male mice (Figures S7O and S7P). In addition,
425 a reduced hypoglycemic effect of insulin was detected in male KO^{Myf5} mice upon insulin
426 tolerance test (ITT) assays (Figures S7Q and S7R).

427 Overall, these results indicate that *tp53inp2* ablation in brown adipocyte precursor cells
428 results in the thermogenic dysfunction of iBAT, which impacts energy balance and
429 contributes to weight gain. In addition, *tp53inp2* ablation causes alterations in glucose
430 tolerance as a consequence of a reduced capacity to respond to insulin.

431

432 ***TP53INP2 is essential for diet-induced thermogenesis.***

433 Next, we studied the impact of *tp53inp2*-deficient BAT in the absence of cold stress.
434 Under increased environmental temperature conditions (30ºC), cold-induced
435 thermogenesis is abolished, but there is still a thermogenic component induced by diet, a
436 process that is specific to brown adipocytes. Thus, we housed two groups of mice at 30ºC
437 for 5 months, starting just after weaning. One group was fed a standard chow diet (CD),
438 while the other received a high-fat diet (HFD), potentially inducing an increase in
439 thermogenic capacity due to the high consumption of fat [33, 34].

440 Exposure of mice to 30ºC and to a CD diet resulted in no differences in body weight or
441 in iBAT weight between wild-type and KO^{Myf5} groups, but a slight increase in the total

fat mass of the KO^{Myf5} mice was detected (Figures 7A-C). When animals were challenged with a HFD at 30ºC, KO^{Myf5} mice again showed a greater body weight (Figure 7A), together with an increased total fat mass, iBAT mass, and size of white adipose depots (Figures 7B-E) compared to control littermates. No changes in lean mass were detected between genotypes (Figure 7F).

These results further support the view that TP53INP2 deficiency in BAT decreases non-shivering adaptive thermogenesis and, consequently, induces fat accumulation. Morphological analysis of iBAT showed again that brown adipocytes were unilocular and undistinguishable between groups under 30ºC conditions and with a standard diet (Figures 7G-I). HFD administration increased the appearance of multilocular adipocytes in control mice in keeping with active thermogenesis. This effect was blunted in KO^{Myf5} mice, as reflected by an increase in the average LD size compared to control animals. (Figures 7G-I). Increased environmental temperature blocks the effect of *tp53inp2* ablation, and argues strongly that this is a BAT specific effect only present under conditions of thermogenic activation, as it is prolonged feeding with HFD. Thus, 30ºC acclimated mice were fed either with CD or HFD and then were challenged with NE to measure whole body ΔVO_2. Interestingly, the results obtained clearly demonstrate that diet-induced maximal thermogenic capacity is also impaired in *tp53inp2* KO mice (Figures 7J and 7K).

Thermogenesis modulates TP53INP2 expression in brown adipose tissue.

Based on the data indicating that TP53INP2-dependent autophagy modulates BAT metabolism and brown adipose differentiation, we analyzed whether TP53INP2 expression is modulated upon enhanced BAT function. Mice subjected to a HFD showed

enhanced expression of *Tp53inp2* (2.3-fold) and *Ucp1* (Figure 8A) in iBAT, suggestive of active diet-induced thermogenesis, as previously described [33, 34]. A HFD also induced the expression of TP53INP2 and UCP1 proteins (Figures 8B and 8C). In order to evaluate whether HFD-induced increase in TP53INP2 expression is a mechanism that prevents the excessive accumulation of fat *in vivo*, we fed LoxP and KO^{Myf5} mice with HFD for 16 weeks. Under these conditions, *tp53inp2* KO mice gained more body weight and fat mass compared with control littermates already at 8 weeks after HFD, and without alterations in lean mass (Figures 8D-F and S8A). 16 weeks after, the iBAT and ingWAT adipose depots were significantly expanded in KO^{Myf5} mice, but pgWAT showed similar weight between genotypes (Figures S8B-D). As a result, fat mass gain between 8 and 16 weeks of HFD was 3-fold greater in KO^{Myf5} mice compared to controls (Figure 8G). Under these conditions, liver weight was also increased in *tp53inp2* KO animals (Figure S8E), while muscles weight was unchanged (Figure S8F). All these data indicate that TP53INP2 expression in iBAT prevents the development of obesity in mice and its metabolic complications.

Low environment temperature is another situation characterized by enhanced brown adipose thermogenesis. Exposure of mice to cold (4°C for 10 h) also acutely upregulated the expression of *Tp53inp2* (2.2-fold), followed by the expected increase in *Ucp1* and *Ppargc1a* mRNA (Figure 8H) [35-37]. The converse situation, BAT thermogenesis inactivation in C57/BL6 mice induced by increasing environmental temperature to 30ºC versus standard housing conditions (22ºC) showed marked downregulation of *Tp53inp2* in BAT (Figure 8I), in parallel with the expected low expression of thermogenic genes such as *Ucp1*, *Ppargc1a* and *Prdm16* [24, 25, 38] under these conditions (Figure 8I).

To further confirm that *Tp53inp2* expression was modulated specifically in brown adipocytes, we studied the mRNA levels of this gene in cultured brown adipocytes.

Differentiation of human or mouse brown preadipocytes markedly induced TP53INP2 mRNA and protein levels (Figures 8J and S8G-K). In addition, brown adipocytes were stimulated or not with the β3-adrenergic agonist CL for 4 h. Indeed, *Tp53inp2* expression was markedly increased (56%), alongside the induction of *Ucp1* and *Ppargc1a* (Figure S8L). Intracellular stimuli such as the cAMP analogues 8-bromo-cAMP (8Br) and dibutyryl-cAMP (dcAMP) or the adenylyl cyclase activator forskolin (FSK) were also capable to dramatically induce *Tp53inp2* mRNA and protein levels in mature human PAZ6 brown adipocytes (Figures 8K, 8L and S8M). Our results suggest that the modulation of TP53INP2 expression is part of a mechanism aimed to activate PPARG and mitochondrial biogenesis upon BAT recruitment both in human and in murine cells.

Discussion

In this work, we document that TP53INP2-dependent autophagy plays a relevant role in brown adipose cell metabolism and differentiation. Disruption of TP53INP2-dependent autophagy reduced brown adipogenesis in cultured cells, and *in vivo tp53inp2* ablation in BAT caused dysregulated gene expression and enhanced lipid accumulation in brown adipocytes. This was the result of decreased UCP1 protein and reduced BAT non-shivering thermogenesis, leading to a positive energy balance. Furthermore, TP53INP2 also maintains the differentiation state of brown adipocytes in adult mice. Mechanistically, TP53INP2 promotes the autophagic degradation of the PPARG co-repressor NCOR1, which stimulates PPARG activity and adipogenesis in brown preadipocytes. Our data manifest the relevance of autophagy activity in the control of BAT metabolism, and emphasize the potential use of autophagy-directed drugs to treat obesity and related metabolic diseases.

Studies using mouse brown preadipocytes and cells undergoing differentiation have revealed that TP53INP2 is required for the autophagy-mediated degradation of NCOR1 to maintain PPARG activity. Thus, TP53INP2 repression is linked to impaired autophagy flux and increased NCOR1 protein levels in the nuclear compartment. In addition, TP53INP2 overexpression enhanced autophagic flux, NCOR1 degradation through autophagy, and in parallel, reduced NCOR1 nuclear abundance. The effects of TP53INP2 overexpression were linked to its ability to trigger autophagy and mutations on its LIR motif cancelled them. These results are coherent with prior data indicating that both NCOR1 and TP53INP2 proteins localize on the nucleus under basal conditions and they are shuttled to the cytosol upon autophagy activation [17, 29, 30, 39, 40]. Moreover, cells with altered autophagy exhibit either retention of NCOR1 in the nucleus or aberrant NCOR1 accumulation on the cytosol [29, 30, 41]. Notably, the defective PPARG activity

detected in TP53INP2-deficient cells was ameliorated upon NCOR1 down-regulation. In all, our data reveal a causal connection between the modulation of NCOR1 protein levels by TP53INP2 and the observed PPARG transcriptional activity.

Based on the results documenting a physical interaction between TP53INP2 and NCOR1, we propose that TP53INP2 facilitates NCOR1 translocation to autophagosomes for its degradation. As to the potential mechanisms by which TP53INP2 sense a thermogenic stimulus and promotes the nuclear exit of NCOR1, they remain unknown. Perhaps relevant to this question, are the following observations: i) TP53INP2 shuttles between the nucleus and the cytosol, and rapamycin or amino acid starvation causes the rapid recruitment of nuclear TP53INP2 to the cytosol in cells [17, 42]; ii) TP53INP2 binds to Atg8-family proteins such as GABARAPL2 or LC3, and this is key for the binding of LC3 to ATG7 proteins to initiate autophagy [17, 42, 43]; and iii) SIRT1-dependent deacetylation of LC3 enables its interaction with TP53INP2, promoting its recruitment to the cytosol [44]. Based on these observations, we propose that similarly to what occurs for LC3, NCOR1 requires TP53INP2 for its exit from the nucleus, and its subsequent engagement into autophagic degradation upon a thermogenic stimulus.

Depletion of the autophagic protein ATG7 in white and brown adipocytes has been reported to reduce interscapular BAT mass, lipid droplet deposition, and to increase beta-oxidation [8]. Ablation of *atg7* in $MYF5^{+}$ precursor cells, revealed a role of autophagy on the differentiation of brown preadipocytes [9], and BAT from KO mice had bigger lipid droplets and diminished levels of UCP1 and mitochondrial markers [9]. Further mechanistic studies nicely documented that depletion of the autophagy receptor protein SQSTM1 in brown adipocytes attenuated the expression of PPARGC1A and UCP1 in BAT and decreased energy expenditure in mice [10, 11]. These effects were not directly associated to impaired autophagic flux, but consequence of the inhibition of the

551 transcription factor ATF2 or the reduction in the formation of PPARG-RXR heterodimers
552 [11, 12]. Thus, the direct mechanisms that link autophagic activity with brown fat
553 differentiation remained unknown. The results obtained in the present study support the
554 requirement of autophagy for the optimal differentiation of brown adipocytes, and
555 autophagy inhibition with chloroquine treatment or by TP53INP2 deficiency reduced
556 adipogenic markers such as UCP1, PPARG2 and PPARG1. In this work we expand our
557 view on the mechanistic role of autophagy on BAT metabolism, and we document that
558 TP53INP2-dependent autophagy controls NCOR1 abundance and PPARG activity in
559 brown adipose cells. In this connection, we support the view that TP53INP2 is involved
560 in constitutive autophagy, as TP53INP2 depleted cells displayed reduced autophagic flux
561 determined by LC3B-II accumulation upon bafilomycin A_1 treatment, and TP53INP2
562 overexpressing cells showed the opposite phenotype. However, this does not rule out the
563 possibility that TP53INP2 is involved in the selective autophagic degradation of NCOR1,
564 which will require further analysis.

565 Our data have revealed that the TP53INP2 protein is a positive regulator of brown
566 adipogenesis and that it maintains brown adipocyte identity in adult mice through
567 PPARG activation. Ablation of *tp53inp2* in adult mice cause BAT dysfunction, altered
568 expression of metabolic genes, and obesity. In keeping with these data, we have also
569 documented that TP53INP2 deficiency in brown preadipocytes reduces the expression of
570 crucial brown adipose differentiation genes such as *Prdm16*, *Ucp1* or *Ppargc1a*, and
571 UCP1 protein levels in iBAT. Thus, TP53INP2 induces BAT-specific maximal
572 thermogenic capacity and prevents the development of obesity in mice. However,
573 TP53INP2 seems to be dispensable for the embryonic development of BAT. This
574 phenotype is similar to what detected when genes that are essential in BAT differentiation
575 where specifically ablated, such as *Prdm16*, *Tyk2* or *Stat3* [26, 45], and suggests that

under conditions of TP53INP2 deficiency, alternative pathways that maintain adipogenesis may be triggered in brown preadipocytes *in vivo*. In this connection, we have clearly documented that *tp53inp2* ablation reduces the differentiation state of brown adipocytes without altering the total number of adipocytes in BAT, and adipocytes displayed hypertrophy as a consequence of reduced UCP1-mediated uncoupling activity and enlargement of lipid droplets. This is in agreement with the described role of PPARG in BAT, which is not essential for its commitment but rather for its maturation [15].

Of note, TP53INP2 has opposite effects on adipose differentiation in white and brown preadipocytes. In this regard, this protein has been reported to block white adipose differentiation by enhancing TCF activity through a process that depends on the sequestration of GSK3B in an endosomal compartment and the accumulation of CTNNB1/β-catenin [20]. Another study using bovine white preadipocytes also documented an adipogenic role of TP53INP2 [46]. In this study, we document that TP53INP2 has a stimulatory effect in brown preadipocytes through the activation of PPARG transcriptional activity. Based on the current evidence, we propose that the maintenance of high TP53INP2 activity in white and brown adipose depots prevents the development of obesity in mice.

TP53INP2 promotes BAT-specific diet-induced thermogenesis. In this connection, *tp53inp2* ablation reduced BAT thermogenesis, and this was followed by enhanced adiposity in mice. The repression of TP53INP2 expression in conditions of increased environmental temperature, when combined with maintained or increased food intake, may contribute to the development of obesity in mice. Furthermore, HFD-induced TP53INP2 expression in BAT represents an adaptive mechanism to prevent an excessive accumulation of body fat under obesogenic conditions. Thus, the induction or activation of TP53INP2 in the absence of cold-stress through a HFD-independent stimulus could be

601 an efficient tool through which to increase thermogenic activity at the whole-body level,
602 thus preventing obesity.

603 Interestingly, our findings indicate that the expression of TP53INP2 in interscapular BAT
604 is upregulated by conditions characterized by enhanced BAT thermogenic activity,
605 namely exposure to cold or a HFD. In contrast, the expression of TP53INP2 is repressed
606 under 30ºC environment, i.e., a condition with no need to generate heat. Sympathetic
607 nerves directly control BAT thermogenesis through the action of NE. In this regard, cold
608 exposure or a chronic HFD cause the sympathetic nervous system to release NE and to
609 activate the β-adrenergic receptors present on the surface of brown adipocytes [3, 6, 47-
610 49]. Given these findings and the observations that a β3-adrenergic agonist enhances
611 TP53INP2 expression in mouse brown adipocytes, and that cAMP analogs increase
612 TP53INP2 expression in human PAZ6 adipocytes, we propose that the adrenergic-
613 mediated PKA signaling pathway is involved in the upregulation of TP53INP2 in BAT
614 under *in vivo* conditions. Overall, our results unravel a novel protein target that, if
615 selectively activated, could increase BAT thermogenic metabolism and prevent obesity
616 and metabolic disorders associated to this condition.

Materials and Methods

Mice strains

The KO^{Myf5} mouse line was generated by crossing homozygous *Tp53inp2 LoxP*$^{+/+}$ mice [19] with a Cre-recombinase-expressing mouse strain under the control of the *Myf5* promoter (The Jackson Laboratory, 007893). Experimental groups contained *LoxP*$^{+/+}$ *Cre negative* (LoxP) and *LoxP*$^{+/+}$ *Cre positive* mice (KO^{Myf5}).

The total *tp53inp2* knockout (KO^{Ubc}) mouse line was obtained by crossing homozygous *Tp53inp2 LoxP*$^{+/+}$ mice with a mouse strain expressing the Cre-recombinase under the control of the *Ubc* promoter (UBC-Cre-ERT2), as previously described [20].

Skeletal muscle specific *tp53inp2* knockout mouse line (KO^{Mlc1}) was generated by crossing homozygous *Tp53inp2 LoxP*$^{+/+}$ mice with a mouse strain with Cre-recombinase expression under the control of the *Myl1* (myosin, light polypeptide 1) promoter [19].

Mice were bred in a C57BL/6J genetic background, kept under a 12-h dark-light period, and provided with a standard chow-diet and water *ad libitum*. When indicated, animal cages were placed inside a thermostatic enclosure at 30°C for 5 months, and/or were fed a high-fat diet (HFD) for the indicated period (60 kcal% Fat, Research Diets Inc.).

Body composition analysis

Mouse body composition was measured using magnetic resonance with the EchoMRI™ Body Composition Analyzer.

Histology

Interscapular BAT (iBAT) samples were fixed overnight in 4% PBS-buffered formalin (PanReac, 252931). Fixed samples were dehydrated and embedded in paraffin. iBAT

sections were stained with hematoxylin and eosin (H&E), and lipid droplet (LD) area and LD number were quantified with Ilastik software. For immunohistochemistry studies, iBAT sections were stained with the rabbit polyclonal anti-UCP1 (Abcam, ab10983) followed with the Alexa Fluor Plus 647 Goat anti-Rabbit IgG (H+L) (Invitrogen, A32733) as a marker of brown adipocytes. Wheat germ agglutinin (WGA), Alexa Fluor® 488 conjugate (Invitrogen, W11261) was used to label plasma membranes. Nucleus were stained with DAPI. Specificity of staining was confirmed by staining with a rabbit IgG isotype control (Abcam, ab37415). Fluorescent images were acquired with a NanoZoomer-2.0 HT C9600 digital scanner (Hamamatsu, Photonics, France) equipped with a 20X objective and coupled to a mercury lamp unit L11600-05 and using NDP.scan2.5 software U10074-03 (Hamamatsu, Photonics, France). DAPI signal of all the samples has been acquired with the filter DAPI350 with an exposure time of 13 ms and a gain of 6. WGA-488 signal of all the samples has been acquired with the FITC filter with an exposure time of 28 ms and a gain of 4. UCP1-647 signal of all the samples has been acquired with the Cy5 filter with an exposure time of 57 ms and a gain of 8. All images were visualized with the NDP.view 2 U123888-01 software (Hamamatsu, Photonics, France) with a gamma correction set at 1.0 in the image control panel of the software. Slides were evaluated in blind manner, using QuPAth software[50] for the UCP1-647 intensity with the "Add intensity features", HALO® imaging analysis software (Indica Labs) software using the "Highplex IF v4.1.3" analysis for the nuclei count and the "DenseNet AI V2 (plugin)" classifier followed by the "Highplex IF v4.1.3" analysis independently trained for the detection of the adipocytes following the WAG labeling. The classifier algorithm was trained to segment the image between "adipocytes" and "rest of the tissue + background". Selection of tissue was performed manually, and

663 tissue artefacts such as broken areas were excluded. Finally, the number of adipocytes
664 was determined with a 25-1000 μm^2 cell size filter.

665 ***Indirect calorimetry and thermogenesis assessment***

666 Oxygen consumption (VO_2), carbon dioxide production (VCO_2) and locomotor activity
667 were measured using an indirect calorimetry system (Oxymax, Columbus Instrument).
668 Energy expenditure ($3.815*VO_2+1.232*VCO_2$), VO_2 and VCO_2 were calculated with an
669 adjusted body weight of 29.4714 g (KO^{Myf5}) or 27.0625 g (KO^{Mlc1}), determined using
670 ANCOVA. The respiratory exchange ratio (RER, VCO_2/VO_2), glucose oxidation
671 ($4.545*VCO_2-3.205*VO_2$), and lipid oxidation ($1.672*(VO_2-VCO_2)$) were calculated
672 using the respective formulas.

673 Norepinephrine (NE)-induced maximal thermogenic capacity was assessed in mice that
674 had been acclimated either to 22°C or to 30°C. The animals were anesthetized by an
675 intraperitoneal injection of pentobarbital (80 mg/kg), maintained inside the 30°C
676 enclosure, and placed inside the metabolic chamber to measure basal respiration. After
677 20 min, the cage was opened and mice were injected with a subcutaneous dose of NE
678 (Sigma-Aldrich, A0937; 1 mg/kg) to measure NE-induced respiration. Data are presented
679 as increase in oxygen consumption (ΔVO_2) from basal respiration. For statistical
680 comparison of the curves (Figures 6D and 7J), we fitted a random slope mixed effects
681 model separately for measures taken at 22ºC and 30ºC that take into consideration the
682 longitudinal structure of the data. We considered the ΔVO_2 as the dependent variable.
683 The time, genotype (LoxP or KO^{Myf5}) and interaction of the two were taken as
684 independent variables. The difference in time linear effect between KO^{Myf5} and LoxP was
685 estimated by a REML procedure using the lme function from the nlme R package [51].
686 Although only time points between 56 min to 100 min were considered for this analysis,

687 the results obtained were consistent for other starting times. Diet-induced maximal
688 thermogenic capacity was measured with the same methodology, using mice that were
689 acclimated to 30ºC and fed either a CD or a HFD.

690 ***Glucose and insulin tolerance tests***

691 Intraperitoneal GTT or ITT were performed in male and female mice at 3 months of age
692 housed at 22ºC. For the GTT, mice were fasted 16 h before the administration of 2 g/kg
693 glucose dose. Blood glucose levels were measured from time 0 to 150 min after glucose
694 injection. At determined points, blood was also collected with Microvette® tubes
695 (Starstedt, 16444), for the posterior determination of plasma insulin levels using an Ultra
696 Sensitive Mouse Insulin ELISA kit (Cristal Chem, 90080) following manufacturer
697 instructions. ITT was performed after 4 h of fasting with an insulin (Lilly, Humalog® 100
698 U/ml) dose of 0.7 U/kg. Blood glucose levels were monitored as for the GTT.

699 ***Food and water intake***

700 Mice were placed individually in metabolic cages and allowed to acclimate to the new
701 environment for 48 h. Food and water intake measurements per mouse were collected
702 every 24 h over two consecutive days.

703 ***High-resolution respirometry***

704 The respiration of permeabilized muscle fibers and BAT mitochondria was measured at
705 37°C in MiR05 buffer by high-resolution respirometry with the Oxygraph-2k (Oroboros
706 Instruments, Innsbruck, Austria). iBAT was homogenized in a sucrose buffer (250 mM
707 sucrose [Sigma-Aldrich, 84100], 50 mM KCl, 5 mM EDTA, 5 mM $MgCl_2$, 1 mM
708 $Na_4P_2O_7$, pH 7.4) and centrifuged at 740*g* for 5 min. The supernatant was centrifuged at
709 9,000*g* for 15 min and the mitochondrial pellet was washed and resuspended in sucrose

buffer. Tibialis anterior fibers were prepared and permeabilized as previously described [52]. All respiration measurements were made on fresh tissues immediately after dissection, and each sample was assayed in duplicate. Oxygen flux (shown as "Leak" in figures) was measured with 2 mM malate (Sigma-Aldrich, M1000) and 10 mM glutamate (Santa Cruz Biotechnology, sc-211703), in the absence of ADP (Sigma-Aldrich, A5285). Complex I-derived mitochondrial respiration (denoted as "C I" in figures) was measured with the addition of ADP (1 mM for iBAT mitochondria and 2.5 mM for permeabilized fibers). Finally, succinate (Sigma-Aldrich, S2378) was added to a final concentration of 10 mM to measure electron flow through both complex I and II (denoted as "C I+II" in the figures). Non-mitochondrial respiration levels were subtracted and determined by the addition of 2.5 μM antimycin A (Sigma-Aldrich, A8674). In order to ensure the integrity of the outer mitochondrial membrane, 10 μM CYCS/cytochrome c (Sigma-Aldrich, C2037) was added, and no stimulation of respiration was observed.

DNA and RNA extraction and qPCR

Total DNA was extracted from mouse iBAT. Tissue was digested with proteinase K (Merck Life Science S.L.U., 03115801001) and total DNA was purified using DNeasy Blood & Tissue Kit (Qiagen, 69504).

Total RNA was extracted from mouse tissues or mouse cell cultures by homogenization with TRIzol reagent (Thermo Fisher Scientific, 15596018) and purification with PureLink™ RNA Mini Kit (Thermo Fisher Scientific, 12183018A). An amount of 2 μg of RNA was reverse-transcribed with the SuperScript™ II RT kit (Thermo Fisher Scientific, 18064014). Gene expression was analyzed by quantitative real-time PCR performed using Power SYBR™ Green PCR Master Mix (Thermo Fisher Scientific, 4367659) and ABI Prism 7900 HT real-time PCR system (Applied Biosystems).

Arpc/*Arp* was used as internal control for normalization. The primers used for qPCR are listed in Table S1.

Human Paz6 cells were lysed in RLT buffer containing 1% β-ME. RNA extraction was carried out using RNeasy Qiagen Kit (Qiagen, 74004) following manufacturer's instructions. RNA concentration was quantified using an Epoch™ 2 microplate reader. cDNA was generated from 1 µg of isolated RNA using M-MLV reverse transcriptase (Promega, M1701) and diluted 1:20 for use in 15 µL qPCR reactions using SYBR® Green PCR master mix (Applied Bioscience, 4344463) and run on the Applied Biosystems StepOnePlus™ system. The geometrical average of 4 different genes (*GAPDH*, *ACTB*/*β-actin*, *HPRT* and *TBP*) was used as an internal control, following an already described normalization method [53].

Transcriptomic analysis

Microarray services were provided by the IRB Barcelona Functional Genomics and Biostatistics/Bioinformatics Core Facilities, as described [20], including quality control tests of total RNA using an Agilent Bioanalyzer and nanodrop spectrophotometry. Briefly, the complementary DNA library was prepared and amplified from 25 ng total RNA using the TransPlex® Complete Whole Transcriptome Amplification Kit (Sigma-Aldrich, WTA2) with 17 cycles of amplification. cDNA (8 µg) was subsequently fragmented by DNaseI and biotinylated by terminal transferase obtained from the GeneChip Mapping 250K Nsp Assay Kit (Affymetrix, 900766). The hybridization mixture was prepared following Affymetrix's protocol. Each sample was hybridized to a Mouse Genome 430 PM strip (Affymetrix, 901570). Arrays were washed and stained in a Fluidics Station 450 (Fluidics protocol FS450_002) and scanned in a GeneChip Scanner

757 3000 (both Affymetrix), following the manufacturer's recommendations. CEL files were
758 generated from DAT files using GCOS software (Affymetrix).

759 Microarray samples were processed using the affy [54] and affyplm packages [55] from
760 Bioconductor [54]. Raw CEL files were normalized using RMA background correction
761 and summarization [56]. Technical metrics PM median, PM interquartile range (IQR),
762 RMA IQR and RNA degradation described in [57] were computed and recorded as
763 additional features for each sample. Differential expression between *tp53inp2* KO vs.
764 LoxP conditions was determined using the moderated t-statistics by empirical Bayes
765 shrinkage method [58]. Batches representing the strip and Eklund metric RNA
766 degradation were included as adjusting variables in the model to correct for technical
767 variability. The moderated t-statistic information (positive change when *tp53inp2* KO
768 was higher than LoxP and negative change when *tp53inp2* KO was lower than LoxP) was
769 considered to rank all genes in the genome, and Gene set enrichment analysis (GSEA)
770 was performed using the Broad Institute's implementation [59] on the KEGG (Kyoto
771 Encyclopedia of Genes and Genomes) collection [60].

772 We downloaded paired-end RNA-seq data from the GSE86338 study [27]. Only samples
773 GSM 2300503 (22°C 1), GSM 2300504 (22°C 2), GSM 2300505 (30°C 1), and GSM
774 2300506 (30°C 2) were considered for normalization and data analysis. Files were aligned
775 against the mm10 genome with STAR 2.3.0e in strand-specific paired-end mode with
776 default parameters [61]. Alignments were sorted and indexed with sambamba v0.5.1 [62].
777 Counts per genomic feature were computed with the R package casper [63] function
778 wrapKnown. A quantile normalization was applied to the resulting rpkm expression
779 matrix. Differential expression between 30ºC vs. 22ºC conditions was analyzed on the
780 normalized data using the moderated t-statistics by the empirical Bayes shrinkage method

781 [58]. A size factor that measured the total number of reads per sample was included in
782 the model as an adjusting variable.

783 We compared the differential expression results obtained from the two transcriptomic
784 analyses, the 30ºC vs 22ºC and *tp53inp2* KO vs LoxP contrasts, by performing a GSEA
785 (33). We used as background ranked list the moderated t-statistics of the 30ºC/22ºC
786 contrast and as testing gene-sets two signatures of 100 genes containing the most
787 KO/LoxP differentially expressed genes (ordered by the t-statistic), distinguishing
788 between up- and downregulated genes.

789 ***Cell culture***

790 Primary brown preadipocytes were isolated from iBAT as previously described [22].
791 Briefly, 6-8 iBAT depots from 1-month-old *Tp53inp2 LoxP*$^{+/+}$ or *Tp53inp2 LoxP*$^{+/+}$
792 *UBC-Cre-ERT2* mice were minced and digested in collagenase buffer at 37°C for 30-40
793 min (1 mg/ml collagenase A [Sigma-Aldrich, 10103578001], 4% BSA fraction V [Sigma-
794 Aldrich, A9647] and penicillin-streptomycin 100 U/ml in HBSS medium [Thermo Fisher
795 Scientific, 14025050]). Stromal vascular fraction cells were seeded in primary culture
796 medium (DMEM: Hams F12 (1:1) [Thermo Fisher Scientific, 11320074], 10% FCS, 20
797 mM HEPES, pH 7.4 and penicillin-streptomycin 100 U/ml) and immortalized through
798 retroviral expression of SV40 large-T antigen (Addgene, 13970; deposited by Thomas
799 Roberts). Control (C) and *tp53inp2* KO preadipocytes were generated by GFP or Cre-
800 GFP adenoviral infection, respectively, and sorted by flow cytometry against GFP
801 fluorescence. Parallel cultures of immortalized brown preadipocytes were also used to
802 generate TP53INP2 deficiency model. Lentivirus encoding for a siRNA scramble or
803 against *Tp53inp2*, as control (SCR) or knockdown (KD), were produced in HEK 293T
804 cells (ATCC, CRL-11268) as reported [18]. Transduced cells were selected based on GFP

fluorescence and sorted with FACSAria Fusion flow cytometer. Acute TP53INP2 repression was induced by transfection with siRNAs using Lipofectamine 3000 (Thermo Fisher Scientific, L3000015). Transfections included 15 nM of MISSION siRNA Universal Negative Control #1 (Sigma-Aldrich, SIC001), si*Tp53inp2* #1 (Sigma-Aldrich, SASI_Mm01_00032790) or si*Tp53inp2* #2 (Sigma-Aldrich, SASI_Mm02_00348576).

HA-PPARG2-overexpressing brown preadipocytes were generated by retroviral infection with pBABE-empty-Puro (Addgene, 1764; deposited by Hartmut Land, Jay Morgenstern and Bob Weinberg) or pBABE-PPARG2-Puro (Addgene, 1764; deposited by Bruce Spiegelman) and puromycin selection (Santa Cruz Biotechnology, sc-108071; 3 μg/ml). TP53INP2 was ablated in these cells following the same methodology described above.

TP53INP2 or TP53INP2^{W35,I38A} mutant (TP53INP2-LIR) [17, 18] were subcloned into a lentiviral Gateway destination vector, and empty vector was used as control (Addgene; 19067 and 17478, deposited by Eric Campeau and Paul Kaufman). Lentiviral particles were produced in HEK 293T cells and used to infect brown preadipocytes. Infected cells were selected with neomycin (Thermo Fisher Scientific, 10131-027; 400 μg/ml).

Cells were maintained in proliferation medium (DMEM, 10% FBS, 20 mM HEPES, pH 7.4 and penicillin-streptomycin 100 U/ml). Differentiation was achieved by growing cells to confluence for 3 days in differentiation medium (proliferation medium supplemented with 20 nM insulin and 1 nM T3 [Sigma-Aldrich, I1882 and T6397]). Subsequently, differentiation was triggered by induction medium (day 0) (differentiation medium supplemented with 0.5 μM dexamethasone, 0.125 mM indomethacin and 0.5 mM IBMX [Sigma-Aldrich, D2915, I8280 and I7018]) for 48 h. Cells were then switched again to differentiation medium for 7 days. When indicated, adipocytes were treated with 1 μM CL-316,243 (Sigma-Aldrich, C5976), 1 μM 4-hydroxy-tamoxifen (Sigma-Aldrich,

H7904), or 15 μM chloroquine (Sigma-Aldrich, C6628). Autophagy flux was assessed upon 200 nM bafilomycin A_1 (Santa Cruz Biotechnology, sc-201550) treatment for 4 or 6 h.

The human immortalized brown cell line Paz6 was provided by A Vidal-Puig and was cultured and differentiated as previously described [64]. When incubated with different compounds i.e 8-Br cAMP, Forskolin and dcAMP (Sigma-Aldrich, B7880, F3917 and D0260), the mature adipocytes were kept overnight in differentiation medium without serum and then treated with the different agents at the concentration of 10^{-5} M for 4 h. Then the cells were harvested for RNA or protein extraction.

Monoclonal antibody production

BALB/c mice were immunized, three times, by intraperitoneal injection with the purified peptide (40 μg) SPPAPSLMDESWFVTPPAC covalently linked to KLH, corresponding to human TP53INP2 (residues 60-78). Hybridomas were produced by fusing spleen cells with myeloma cells using polyethylene glycol in mHAT+HFCS-RPMI medium and following standard hybridoma techniques. Supernatants of the hybridomas were screened by indirect ELISA on polystyrene plates coated with the peptide. Bound antibodies were detected using horseradish peroxidase-labelled goat anti-mouse antibody (Dako, P 0447). The positive hybridomas were subcloned by limiting dilution, and the specificity of antibodies was validated by western blot assays.

Protein extraction and western blot

Total homogenates were extracted with RIPA buffer (50 mM Tris-HCl pH 8.0, 150 mM NaCl, 1% NP-40 [Sigma-Aldrich, I3021], 0.1% SDS and 1 mM EDTA) or lysis buffer (50 mM Tris-HCl pH 7.5, 150 mM NaCl, 1% Triton X-100 and 1 mM EDTA) from cell

cultures or iBAT respectively, with freshly added phosphatase inhibitors 1 mM Na_3VO_4, 5 mM $Na_4P_2O_7$ and 50 mM NaF, and protease inhibitor cocktail (Complete-Mini; Roche, 11836153001). After centrifugation at 16,000*g* for 20 min at 4°C, supernatants were quantified by the BCA protein Assay (Thermo Fisher Scientific, 23225). The same amount of proteins was resolved in acrylamide gels for SDS-PAGE and transferred to PVDF membranes (Millipore, IPFL00010). The following primary antibodies were used: PPARG (H-100) and LMNA/lamin A/C (N-18) (Santa Cruz Biotechnology, sc-7196 and sc-6215); UCP1 and MFN2 (Abcam, ab10983 and ab56889); TIMM44 (BD Biosciences, 612582); and NCOR1, LC3B and HA-tag (Cell Signaling Technology, 5448, 2775 and 3724). The TP53INP2 antibody was generated in our laboratory as described. TUBA4A/α-tubulin and ACTB/β-actin (Sigma-Aldrich, T5168 and A1978), and TBP or VCL/vinculin (Abcam, ab818 and ab18058) antibodies or Revert™ 700 Total Protein Stain (LI-COR, 926-11011) were used as loading controls. Proteins were detected by the ECL method and quantified by densitometry using ImageJ, or by NIR-fluorescence detected with LI-COR Odyssey System and measured with Image Studio software.

NE-induced respiration in cultured brown adipocytes

Control and *tp53inp2* KO brown preadipocytes were plated in SeaHorse Bioscience XF24 plates (3,000 cells/well) and induced to differentiate as described above. Mitochondrial respiration was evaluated at day 9 of differentiation. Cells were switched to respirometry medium containing DMEM (Sigma-Aldrich, D5030) supplemented with 1 mM glutamine, 2 mM pyruvate and 5 mM glucose. Oxygen consumption rate was detected under basal and NE-stimulated conditions (1 μM). Non-mitochondrial oxygen consumption was subtracted and measured by adding 2.5 μM rotenone (Sigma-Aldrich, R8875) and 2.5 μM antimycin A. Data are shown as NE-induced mitochondrial respiration.

PPAR transcriptional activity

For transcriptional activity assays brown preadipocytes were transfected with PEI MAX 40K (Polysciences Inc., 24765) or with Lipofectamine 3000 when the reactions contained siRNA. Transfections included 1 μg of the reporter plasmid PPREx3-TK-Luc (kindly provided by Dr. D. Haro, Institute of Biomedicine of the University of Barcelona [IBUB], Barcelona, Spain) and, when indicated, 500 ng of PPARG. siRNAs used, MISSION siRNA Universal Negative Control #1 (Sigma-Aldrich, SIC001) or si*Ncor1* (Sigma-Aldrich, SASI_Mm01_00098740), were transfected with a final concentration of 15 nM. To normalize for transfection efficiency, 100 ng of TK-Renila plasmid (Promega, E2261) was used. Twenty-four hours after transfection, cells were treated, when indicated, with 10 μM rosiglitazone (Sigma-Aldrich, R2408) for an additional 24 h. Extracts were obtained and assays of dual-luciferase reporter were performed (Promega, E2920).

Immunofluorescence

Cells were fixed in 2% paraformaldehyde (PFA) for 3 min and then switched to 4% PFA for a total of 30 min. Permeabilization was performed in 0.1% Triton X-100 in PBS for 15 min and then autofluorescence was blocked using TrueBlack (Biotium, 23007). Coverslips were washed, blocked with 5% FBS for 1 h and then incubated in NCOR1 (dilution 1:200 in blocking buffer; Cell Signaling Technology, 5448) and/or TP53INP2 (dilution 1:250 in blocking buffer) primary antibodies overnight at 4ºC. Cells were then washed with PBS and incubated in Alexa Fluor 568 anti-rabbit (dilution 1:400 in blocking buffer; Invitrogen, A11036) or Alexa Fluor 488 anti-mouse (1:500 in blocking buffer; Invitrogen, A11029) secondary antibodies for 1 h. Cells were washed with PBS and nucleus were stained with Hoechst 33342 (Invitrogen, H3570). Coverslips were washed once again and mounted on microscope slides with Fluoromount (Sigma-Aldrich, F4680).

Confocal images were obtained using Leica TCS SP5 confocal scanning microscope. Z-stacks were acquired with a constant thickness of 0.5 µm. Nuclear to cytosol (N:C) ratio was determined as described [65] using ImageJ software. Briefly, the central section of each cell was used for quantification. Hoechst 33342 staining was used to determine the nucleus perimeter, and GFP fluorescence of the siRNA lentiviral construct to determine the cell perimeter. N:C ratio was calculated dividing the mean intensity of each compartment.

Subcellular fractionation

Nuclear and cytosolic enriched fractions from brown preadipocytes were obtained using NE-PER kit (Thermo Fisher Scientific, 78835) following the manufacturer's recommendations.

Immunoprecipitation

Protein extracts from Flp-In T-REx 293 cells (Thermo Fisher Scientific, R78007) stably expressing empty vector or HA-TP53INP2 were used for immunoprecipitation experiments. Cells were lysed in IP Buffer (20 mM Tris-HCl pH 7.5, 150 mM NaCl, 0.5% NP-40, 1 mM EDTA, 1mM DTT) and centrifuged at 16.000*g* at 4ºC for 20 min. HA affinity isolation was performed incubating protein supernatants with HA-conjugated agarose beads (Sigma-Aldrich, A2095) overnight at 4ºC with rotation. Then, beads were washed five times with one volume each of IP Buffer and finally eluted in Laemmli sample buffer at 95ºC for 5 min. Endogenous NCOR1 immunoprecipitation was carried out with 10 µg of mouse NCOR1 (F-1) antibody (Santa Cruz Biotechnology, sc-515934), or normal mouse IgM (Santa Cruz Biotechnology, sc-3881) as a negative control. Corresponding antibodies were conjugated to Protein L magnetic beads (Thermo Fisher Scientific, 88849) for 2 h at room temperature. Five mg of protein extracts were

925 precleared wit IgM-conjugated Protein L magnetic beads overnight prior to
926 immunoprecipitation. Beads were incubated with precleared lysates, washed and eluted
927 in the same way as HA-beads. Input fractions and immunoprecipitated proteins were run
928 in 4–15% gradient SDS-PAGE gels (Bio-Rad, 4568084), and immunodetection was
929 performed as described.

930 ***Proximity ligation assay***

931 Proximity ligation assays were performed in brown preadipocytes stably expressing
932 TP53INP2, TP53INP2-LIR or empty vector cultured in 96-well imaging plates (Zell-
933 Kontakt, 5242-20) according to the manufacturer's instructions (Duolink® In Situ
934 Detection Reagents FarRed; Sigma-Aldrich, DUO92013). Briefly, cells were fixed with
935 4% PFA, permeabilized with 0.2% Triton X-100 in PBS for 20 min at room temperature
936 and blocked for 30 min at 37ºC. Then, cells were incubated with NCOR1 (dilution 1:200;
937 Cell Signaling Technology, 5448) and TP53INP2 (dilution 1:250) primary antibodies
938 overnight at 4ºC. After that, cells were washed and incubated with PLA probes anti-rabbit
939 PLUS (Sigma-Aldrich, DUO092002) and anti-mouse MINUS (Sigma-Aldrich,
940 DUO092004) for 1 h at 37ºC. Ligation and amplification were performed for 30 and 100
941 min respectively at 37ºC. Finally, cells were stained with Hoechst 33342 (Invitrogen,
942 H3570) for 10 min and kept in citrate buffer (150 mM NaCl, 15 mM sodium citrate, pH
943 7.4). NIKON LIPSI, a high content and high-speed screening platform, equipped with an
944 Eclipse Ti2 inverted microscope, a Yokogawa W1 confocal spinning disk unit, a Prior
945 stage, and two Prime BSI Photometrics sCMOS cameras was used to scan PLA
946 experiments. In every well, at least at 20 fields of view 4 μm deep z-stacks were taken
947 with the Apo LWD 40x water lens of 1.15 NA. The two cameras were used to scan
948 simultaneously Hoechst and Far Red with the spinning disk unit and the 405 and 638
949 lasers. To analyze the number of PLA dots, NIS Elements AR 5.30.05 software was used.

First, z-stacks were maximum intensity projected and the total PLA dots were identified using a bright spot detection method and counted. Nuclei images were processed with Rolling ball background subtraction, thresholded and watersheded.

Study approval

The animal studies followed established guidelines. This project was approved by the Institutional Animal Care and Use Committee of the Parc Cientific de Barcelona (IACUC-PCB), which considered that it complied with standard ethical regulations and met the requirements of current applicable legislation (RD 53/2013 Council Directive; 2010/63/UE; Order 214/1997/GC).

Statistical analysis

Data are presented as means ± SEM. Statistical analysis of the data presented was performed using the Student t-test. Statistical analysis was conducted only to data sets with an $n \geq 3$ independent experiments. Calorimetry data was analyzed using analysis of covariance (ANCOVA).

964 **Acknowledgments**

965 We thank Jorge Manuel Seco, Vanesa Hernández and Laura Alcaide for technological
966 assistance, and Neus Prats, Mònica Aguilera and the Histopathology Core Facility (IRB
967 Barcelona). We also thank the Mouse Mutant and the Functional Genomics Core
968 Facilities (IRB Barcelona). We also want to acknowledge Adrià Caballe and the
969 Biostatistics/Bioinformatics Core Facility (IRB Barcelona) for the analysis of
970 transcriptomic data. We are grateful to Nikolaos Giakoumakis, Anna Lladó and the
971 Advanced Digital Microscopy Core Facility (IRB Barcelona) for help with confocal
972 microscopy and in particular for PLA imaging. A.S. was recipient of a pre-doctoral
973 fellowship from the University of Barcelona. This study was supported by grants from
974 the MINECO (SAF2016-75246R), the Generalitat de Catalunya (Grants 2017 SGR 1015,
975 ICREA Acadèmia), INFLAMES (PIE-14/00045, ISCIII), CIBERDEM, ISCIII,
976 Fundación Ramón Areces (CIVP18A3942), the Fundación BBVA and the Fundació la
977 Marató TV3 (201634-30; 20132330). We gratefully acknowledge institutional funding
978 from the MINECO through the Centres of Excellence Severo Ochoa Award, and from the
979 CERCA Programme of the Generalitat de Catalunya.

References

1. Chouchani ET, Kazak L, Spiegelman BM. New Advances in Adaptive Thermogenesis: UCP1 and Beyond. Cell metabolism 2019; 29:27-37.

2. Nedergaard J, Cannon B. Brown adipose tissue as a heat-producing thermoeffector. Handbook of clinical neurology 2018; 156:137-52.

3. Virtanen KA, Lidell ME, Orava J, Heglind M, Westergren R, Niemi T, et al. Functional brown adipose tissue in healthy adults. The New England journal of medicine 2009; 360:1518-25.

4. Nedergaard J, Bengtsson T, Cannon B. Unexpected evidence for active brown adipose tissue in adult humans. American journal of physiology Endocrinology and metabolism 2007; 293:E444-52.

5. van Marken Lichtenbelt WD, Vanhommerig JW, Smulders NM, Drossaerts JM, Kemerink GJ, Bouvy ND, et al. Cold-activated brown adipose tissue in healthy men. The New England journal of medicine 2009; 360:1500-8.

6. Cypess AM, Lehman S, Williams G, Tal I, Rodman D, Goldfine AB, et al. Identification and importance of brown adipose tissue in adult humans. The New England journal of medicine 2009; 360:1509-17.

7. Becher T, Palanisamy S, Kramer DJ, Eljalby M, Marx SJ, Wibmer AG, et al. Brown adipose tissue is associated with cardiometabolic health. Nature medicine 2021; 27:58-65.

8. Singh R, Xiang Y, Wang Y, Baikati K, Cuervo AM, Luu YK, et al. Autophagy regulates adipose mass and differentiation in mice. The Journal of clinical investigation 2009; 119:3329-39.

9. Martinez-Lopez N, Athonvarangkul D, Sahu S, Coletto L, Zong H, Bastie CC, et al. Autophagy in Myf5+ progenitors regulates energy and glucose homeostasis through control of brown fat and skeletal muscle development. EMBO reports 2013; 14:795-803.

10. Muller TD, Lee SJ, Jastroch M, Kabra D, Stemmer K, Aichler M, et al. p62 links beta-adrenergic input to mitochondrial function and thermogenesis. The Journal of clinical investigation 2013; 123:469-78.

11. Huang J, Linares JF, Duran A, Xia W, Saltiel AR, Muller TD, et al. NBR1 is a critical step in the repression of thermogenesis of p62-deficient adipocytes through PPARgamma. Nature communications 2021; 12:2876.

12. Fischer K, Fenzl A, Liu D, Dyar KA, Kleinert M, Brielmeier M, et al. The scaffold protein p62 regulates adaptive thermogenesis through ATF2 nuclear target activation. Nature communications 2020; 11:2306.

13. Nedergaard J, Petrovic N, Lindgren EM, Jacobsson A, Cannon B. PPARgamma in the control of brown adipocyte differentiation. Biochimica et biophysica acta 2005; 1740:293-304.

14. Koutnikova H, Cock TA, Watanabe M, Houten SM, Champy MF, Dierich A, et al. Compensation by the muscle limits the metabolic consequences of lipodystrophy in PPAR gamma hypomorphic mice. Proceedings of the National Academy of Sciences of the United States of America 2003; 100:14457-62.

15. Barak Y, Nelson MC, Ong ES, Jones YZ, Ruiz-Lozano P, Chien KR, et al. PPAR gamma is required for placental, cardiac, and adipose tissue development. Molecular cell 1999; 4:585-95.

16. Gray SL, Dalla Nora E, Backlund EC, Manieri M, Virtue S, Noland RC, et al. Decreased brown adipocyte recruitment and thermogenic capacity in mice with impaired

peroxisome proliferator-activated receptor (P465L PPARgamma) function. Endocrinology 2006; 147:5708-14.

17. Mauvezin C, Orpinell M, Francis VA, Mansilla F, Duran J, Ribas V, et al. The nuclear cofactor DOR regulates autophagy in mammalian and Drosophila cells. EMBO reports 2010; 11:37-44.

18. Baumgartner BG, Orpinell M, Duran J, Ribas V, Burghardt HE, Bach D, et al. Identification of a novel modulator of thyroid hormone receptor-mediated action. PloS one 2007; 2:e1183.

19. Sala D, Ivanova S, Plana N, Ribas V, Duran J, Bach D, et al. Autophagy-regulating TP53INP2 mediates muscle wasting and is repressed in diabetes. The Journal of clinical investigation 2014; 124:1914-27.

20. Romero M, Sabate-Perez A, Francis VA, Castrillon-Rodriguez I, Diaz-Ramos A, Sanchez-Feutrie M, et al. TP53INP2 regulates adiposity by activating beta-catenin through autophagy-dependent sequestration of GSK3beta. Nature cell biology 2018; 20:443-54.

21. Sancho A, Duran J, Garcia-Espana A, Mauvezin C, Alemu EA, Lamark T, et al. DOR/Tp53inp2 and Tp53inp1 constitute a metazoan gene family encoding dual regulators of autophagy and transcription. PloS one 2012; 7:e34034.

22. Fasshauer M, Klein J, Kriauciunas KM, Ueki K, Benito M, Kahn CR. Essential role of insulin receptor substrate 1 in differentiation of brown adipocytes. Molecular and cellular biology 2001; 21:319-29.

23. Timmons JA, Wennmalm K, Larsson O, Walden TB, Lassmann T, Petrovic N, et al. Myogenic gene expression signature establishes that brown and white adipocytes originate from distinct cell lineages. Proceedings of the National Academy of Sciences of the United States of America 2007; 104:4401-6.

1052 24. Cui X, Nguyen NL, Zarebidaki E, Cao Q, Li F, Zha L, et al. Thermoneutrality
1053 decreases thermogenic program and promotes adiposity in high-fat diet-fed mice.
1054 Physiological reports 2016; 4.
1055 25. Xiao C, Goldgof M, Gavrilova O, Reitman ML. Anti-obesity and metabolic
1056 efficacy of the beta3-adrenergic agonist, CL316243, in mice at thermoneutrality
1057 compared to 22 degrees C. Obesity 2015; 23:1450-9.
1058 26. Harms MJ, Ishibashi J, Wang W, Lim HW, Goyama S, Sato T, et al. Prdm16 is
1059 required for the maintenance of brown adipocyte identity and function in adult mice. Cell
1060 metabolism 2014; 19:593-604.
1061 27. Bai Z, Chai XR, Yoon MJ, Kim HJ, Lo KA, Zhang ZC, et al. Dynamic
1062 transcriptome changes during adipose tissue energy expenditure reveal critical roles for
1063 long noncoding RNA regulators. PLoS biology 2017; 15:e2002176.
1064 28. Perissi V, Rosenfeld MG. Controlling nuclear receptors: the circular logic of
1065 cofactor cycles. Nature Reviews Molecular Cell Biology 2005; 6:542-54.
1066 29. Iershov A, Nemazanyy I, Alkhoury C, Girard M, Barth E, Cagnard N, et al. The
1067 class 3 PI3K coordinates autophagy and mitochondrial lipid catabolism by controlling
1068 nuclear receptor PPARα. Nature communications 2019; 10:1566.
1069 30. Saito T, Kuma A, Sugiura Y, Ichimura Y, Obata M, Kitamura H, et al. Autophagy
1070 regulates lipid metabolism through selective turnover of NCoR1. Nature communications
1071 2019; 10:1567.
1072 31. Mauvezin C, Sancho A, Ivanova S, Palacin M, Zorzano A. DOR undergoes
1073 nucleo-cytoplasmic shuttling, which involves passage through the nucleolus. FEBS
1074 letters 2012; 586:3179-86.

1075 32. Cannon B, Nedergaard J. Nonshivering thermogenesis and its adequate
1076 measurement in metabolic studies. The Journal of experimental biology 2011; 214:242-
1077 53.
1078 33. Mercer SW, Trayhurn P. Effect of high fat diets on the thermogenic activity of
1079 brown adipose tissue in cold-acclimated mice. The Journal of nutrition 1984; 114:1151-
1080 8.
1081 34. Himms-Hagen J, Hogan S, Zaror-Behrens G. Increased brown adipose tissue
1082 thermogenesis in obese (ob/ob) mice fed a palatable diet. The American journal of
1083 physiology 1986; 250:E274-81.
1084 35. Thomas SA, Palmiter RD. Thermoregulatory and metabolic phenotypes of mice
1085 lacking noradrenaline and adrenaline. Nature 1997; 387:94-7.
1086 36. Murholm M, Dixen K, Qvortrup K, Hansen LH, Amri EZ, Madsen L, et al.
1087 Dynamic regulation of genes involved in mitochondrial DNA replication and
1088 transcription during mouse brown fat cell differentiation and recruitment. PloS one 2009;
1089 4:e8458.
1090 37. Carmona MC, Hondares E, Rodriguez de la Concepcion ML, Rodriguez-Sureda
1091 V, Peinado-Onsurbe J, Poli V, et al. Defective thermoregulation, impaired lipid
1092 metabolism, but preserved adrenergic induction of gene expression in brown fat of mice
1093 lacking C/EBPbeta. The Biochemical journal 2005; 389:47-56.
1094 38. Kalinovich AV, de Jong JM, Cannon B, Nedergaard J. UCP1 in adipose tissues:
1095 two steps to full browning. Biochimie 2017; 134:127-37.
1096 39. Sengupta S, Peterson TR, Laplante M, Oh S, Sabatini DM. mTORC1 controls
1097 fasting-induced ketogenesis and its modulation by ageing. Nature 2010; 468:1100-4.

40. Kim K, Pyo S, Um SH. S6 kinase 2 deficiency enhances ketone body production and increases peroxisome proliferator-activated receptor alpha activity in the liver. Hepatology 2012; 55:1727-37.

41. Sinha RA, Singh BK, Zhou J, Xie S, Farah BL, Lesmana R, et al. Loss of ULK1 increases RPS6KB1-NCOR1 repression of NR1H/LXR-mediated Scd1 transcription and augments lipotoxicity in hepatic cells. Autophagy 2017; 13:169-86.

42. Nowak J, Archange C, Tardivel-Lacombe J, Pontarotti P, Pebusque MJ, Vaccaro MI, et al. The TP53INP2 protein is required for autophagy in mammalian cells. Molecular biology of the cell 2009; 20:870-81.

43. You Z, Xu Y, Wan W, Zhou L, Li J, Zhou T, et al. TP53INP2 contributes to autophagosome formation by promoting LC3-ATG7 interaction. Autophagy 2019; 15:1309-21.

44. Huang R, Xu Y, Wan W, Shou X, Qian J, You Z, et al. Deacetylation of nuclear LC3 drives autophagy initiation under starvation. Molecular cell 2015; 57:456-66.

45. Derecka M, Gornicka A, Koralov SB, Szczepanek K, Morgan M, Raje V, et al. Tyk2 and Stat3 regulate brown adipose tissue differentiation and obesity. Cell metabolism 2012; 16:814-24.

46. Zhang W, Li P, Wang S, Cheng G, Wang L, Mi X, et al. TP53INP2 Promotes Bovine Adipocytes Differentiation Through Autophagy Activation. Animals : an open access journal from MDPI 2019; 9.

47. Cypess AM, White AP, Vernochet C, Schulz TJ, Xue R, Sass CA, et al. Anatomical localization, gene expression profiling and functional characterization of adult human neck brown fat. Nature medicine 2013; 19:635-9.

48. Cypess AM, Weiner LS, Roberts-Toler C, Franquet Elia E, Kessler SH, Kahn PA, et al. Activation of human brown adipose tissue by a beta3-adrenergic receptor agonist. Cell metabolism 2015; 21:33-8.

49. Ursino MG, Vasina V, Raschi E, Crema F, De Ponti F. The beta3-adrenoceptor as a therapeutic target: current perspectives. Pharmacological research 2009; 59:221-34.

50. Bankhead P, Loughrey MB, Fernandez JA, Dombrowski Y, McArt DG, Dunne PD, et al. QuPath: Open source software for digital pathology image analysis. Scientific reports 2017; 7:16878.

51. Pinheiro J, Bates D, DebRoy S, Sarkar D, authors (src/rs.f) E, Heisterkamp S, et al. nlme: Linear and Nonlinear Mixed Effects Models. 2019.

52. Sebastian D, Hernandez-Alvarez MI, Segales J, Sorianello E, Munoz JP, Sala D, et al. Mitofusin 2 (Mfn2) links mitochondrial and endoplasmic reticulum function with insulin signaling and is essential for normal glucose homeostasis. Proceedings of the National Academy of Sciences of the United States of America 2012; 109:5523-8.

53. Vandesompele J, De Preter K, Pattyn F, Poppe B, Van Roy N, De Paepe A, et al. Accurate normalization of real-time quantitative RT-PCR data by geometric averaging of multiple internal control genes. Genome biology 2002; 3:RESEARCH0034.

54. Gentleman RC, Carey VJ, Bates DM, Bolstad B, Dettling M, Dudoit S, et al. Bioconductor: open software development for computational biology and bioinformatics. Genome biology 2004; 5:R80.

55. Bolstad BM, Collin F, Brettschneider J, Simpson K, Cope L, Irizarry RA, et al. Quality Assessment of Affymetrix GeneChip Data. In: Gentleman R, Carey VJ, Huber W, Irizarry RA, Dudoit S, eds. Bioinformatics and Computational Biology Solutions Using R and Bioconductor. New York, NY: Springer New York, 2005:33-47.

1145 56. Irizarry RA, Hobbs B, Collin F, Beazer-Barclay YD, Antonellis KJ, Scherf U, et
1146 al. Exploration, normalization, and summaries of high density oligonucleotide array
1147 probe level data. Biostatistics 2003; 4:249-64.
1148 57. Eklund AC, Szallasi Z. Correction of technical bias in clinical microarray data
1149 improves concordance with known biological information. Genome biology 2008; 9:R26.
1150 58. Ritchie ME, Phipson B, Wu D, Hu Y, Law CW, Shi W, et al. limma powers
1151 differential expression analyses for RNA-sequencing and microarray studies. Nucleic
1152 acids research 2015; 43:e47.
1153 59. Subramanian A, Tamayo P, Mootha VK, Mukherjee S, Ebert BL, Gillette MA, et
1154 al. Gene set enrichment analysis: a knowledge-based approach for interpreting genome-
1155 wide expression profiles. Proceedings of the National Academy of Sciences of the United
1156 States of America 2005; 102:15545-50.
1157 60. Kanehisa M, Goto S. KEGG: kyoto encyclopedia of genes and genomes. Nucleic
1158 acids research 2000; 28:27-30.
1159 61. Dobin A, Davis CA, Schlesinger F, Drenkow J, Zaleski C, Jha S, et al. STAR:
1160 ultrafast universal RNA-seq aligner. Bioinformatics 2013; 29:15-21.
1161 62. Tarasov A, Vilella AJ, Cuppen E, Nijman IJ, Prins P. Sambamba: fast processing
1162 of NGS alignment formats. Bioinformatics 2015; 31:2032-4.
1163 63. Rossell D, Stephan-Otto Attolini C, Kroiss M, Stocker A. Quantifying Alternative
1164 Splicing from Paired-End Rna-Sequencing Data. The annals of applied statistics 2014;
1165 8:309-30.
1166 64. Zilberfarb V, Pietri-Rouxel F, Jockers R, Krief S, Delouis C, Issad T, et al. Human
1167 immortalized brown adipocytes express functional beta3-adrenoceptor coupled to
1168 lipolysis. Journal of cell science 1997; 110 (Pt 7):801-7.

65. Kelley JB, Paschal BM. Fluorescence-based quantification of nucleocytoplasmic transport. Methods 2019; 157:106-14.

Figure legends

Figure 1. TP53INP2-dependent autophagy induces brown fat differentiation and maturation. (**A**) LC3B protein abundance and (**B**) LC3B-II fold accumulation in control (C) and *tp53inp2* knockout (KO) mouse brown preadipocytes treated with vehicle (-) or with bafilomycin A_1 (BAF) (+) 200 nM for 6 h (n=3). (**C**) LC3B protein abundance and (**D**) LC3B-II fold accumulation in mouse brown preadipocytes transfected with siRNA control (siSCR) or with different siRNAs targeting *Tp53inp2* (si#1 and si#2) and treated with vehicle (-) or with bafilomycin A_1 (BAF) (+) 200 nM for 4 h (n=5). Panels (**E**) to (**G**): C and KO mouse brown preadipocytes. (**E**) Optical microscopy images at day 9 of differentiation. (**F**) PPARG, UCP1, TIMM44 and MFN2 protein abundance during differentiation (n=3–6). (**G**) Relative mRNA levels of adipogenic and thermogenic genes at day 9 of differentiation (n=4–5). (**H**) LC3B, PPARG and UCP1 protein abundance in adipocytes treated for the last 3 or 7 days of differentiation with 15 μM chloroquine (CQ). Panels (**I**) to (**L**): control (LoxP) and KO^{Myf5} male or female mice at 3 months of age housed at 22°C and subjected to a chow diet (n=7–9 LoxP or KO^{Myf5} mice). (**I**) Weight of iBAT. (**J**) Hematoxylin-eosin (H&E) staining of iBAT sections. (**K**) iBAT sections stained with DAPI (blue), wheat germ agglutinin (WGA, green) and UCP1 (red). (**L**) Expression of adipogenic and thermogenic genes in iBAT. Data are mean ± SEM. *$p<0.05$ vs. control group. Scale bar: 100 μm (H&E images) or 50 μm (DAPI, WGA, UCP1 images).

Figure 2. TP53INP2 maintains the differentiation state of brown adipocytes. Expression of genes in brown adipocytes from (**A**) *tp53inp2* $LoxP^{+/+}$ *Ubc-Cre-ERT2* mice or from (**B**) *Tp53inp2* $LoxP^{+/+}$ *Cre*-negative mice treated with vehicle or with 4-hydroxy-

tamoxifen for 3 days (n=3). Panels (**C**) to (**I**): control (LoxP) and KO^{Ubc} male mice at 8 months of age housed at 22°C and subjected to a chow diet (n=4–8 LoxP or KO^{Ubc} mice). (**C**) Weight of iBAT. (**D**) Hematoxylin-eosin (H&E) staining of iBAT sections, (**E**) lipid droplet (LD) number and (**F**) LD average area measurements. (**G**) iBAT sections stained with DAPI (blue), wheat germ agglutinin (WGA, green) and UCP1 (red), (**H**) number of adipocytes per surface unit and (**I**) adipocyte size distribution measurements. (**J**) Expression of adipogenic and thermogenic genes in iBAT from 4-month-old LoxP and KO^{Ubc} male mice housed at 22°C and subjected to a chow diet (n=4–7 LoxP or KO^{Ubc} mice). Data are mean ± SEM. *p<0.05 vs. control group. Scale bar: 100 μm (H&E images) or 50 μm (DAPI, WGA, UCP1 images).

Figure 3. TP53INP2 stimulates PPARG activity. Panels (**A**) to (**C**): transcriptomic analysis performed in iBAT from LoxP (n=4) or KO^{Myf5} mice (n=4) and compared to transcriptomic analysis from WT mice housed at 22°C (n=2) or 30°C (n=2) in iBAT samples. (**A**) Number of genes upregulated or downregulated (hypergeometric test p-val<0.001). Enrichment plot (GSEA) of the gene sets composed by the (**B**) 100 top up- and (**C**) downregulated genes in iBAT from KO^{Myf5} mice compared to the LoxP group using as background ranked list the 30°C /22°C test statistics (p-val<0.001). GSEA of the most significantly downregulated pathways from Broad Hallmarks by *tp53inp2* ablation in iBAT from (**D**) KO^{Myf5} or (**E**) KO^{Ubc} mice. (**F**) GSEA of PPAR signaling pathway from Kyoto Encyclopedia of Genes and Genomes (KEGG) in the LoxP vs KO^{Myf5} transcriptomic analysis (p-val<0.001). (**G**) PPRE reporter activity in control (SCR) or *tp53inp2* knockdown (KD) brown preadipocytes transfected with empty vector (-) or PPARG (+) and treated with vehicle (-) or with rosiglitazone (+) 1 μM for 24 h (n=5). (**H**) PPRE reporter activity in brown preadipocytes stably expressing empty vector (-) or

HA-PPARG (+), with TP53INP2 endogenous levels (C) or *tp53inp2* knockout (KO) treated with vehicle (-) or with rosiglitazone (+) 1 μM for 24 h (n=3). Data are mean ± SEM. *p<0.05 vs. control group.

Figure 4. TP53INP2 promotes NCOR1 degradation through autophagy. (**A**) NCOR1, LC3B and TP53INP2 protein abundance, (**B**) NCOR1 and (**C**) LC3B-II fold accumulation in control (SCR) or *tp53inp2* knockdown (KD) brown preadipocytes in basal or upon treatment with 200 nM bafilomycin A_1 (BAF) for 4 h (n=9, 7 and 9 respectively). (**D**) NCOR1, LC3B and TP53INP2 protein abundance, (**E**) NCOR1 and (**F**) LC3B-II fold accumulation in control (Empty), TP53INP2 or TP53INP2-LIR stably overexpressing brown preadipocytes in basal (-) or upon treatment with BAF (+) for 4 h (n=4 and 6 respectively). (**G**) NCOR1, LC3B and TP53INP2 protein abundance in day 4 adipocytes transfected at day 2 with siRNA control (SCR) or against *Tp53inp2* in basal (-) or upon treatment with BAF (+) for the last 6 h (n=5, 6 and 6 respectively). (**H**) NCOR1 protein abundance and (**I**) quantification in iBAT from LoxP or KO^{Myf5} male mice at 3 months of age housed at 22ºC and subjected to a chow diet (n=4–7 LoxP or KO^{Myf5} mice).

Figure 5. TP53INP2 promotes the cytosolic recruitment of NCOR1 in an autophagy-dependent manner. Panels (**A**) to (**D**): Control (SCR) or *tp53inp2* knockdown (KD) brown preadipocytes. (**A**) NCOR1 immunostaining and (**B**) nuclear:cytosolic ratio quantification (n=3, each experiment is the average of 17–65 cells). (**C**) NCOR1 protein abundance in total, cytosolic and nuclear homogenates, and (**D**) nuclear NCOR1 quantification (n=5). Panels (**E**) and (**F**): HEK cells stably expressing empty vector (-) or

HA-TP53INP2 (+). (**E**) HA affinity isolation and NCOR1, TP53INP2 and VCL immunoblot in input and pull-down fractions (n=7). (**F**) NCOR1 immunoprecipitation and NCOR1, TP53INP2 and VCL immunoblot in input and immunoprecipitated fractions (n=3). (**G**) Proximity ligation assay (PLA) and nuclei staining (DAPI), and (**H**) PLA dots by nucleus quantification in control (Empty), TP53INP2 or TP53INP2-LIR stably overexpressing brown preadipocytes (representative experiment of n=3 independent experiments). (**I**) PPRE reporter activity in cells transfected with control (siCtr) or *Ncor1* (si*Ncor1*) siRNA and with empty vector (-) or PPARG (+), and treated with vehicle (-) or with rosiglitazone (+) 1 μM for 24 h (n=4). Data are mean ± SEM. *p<0.05 vs. control group. #p<0.05 vs. siCtr. Scale bar: 10 μm.

Figure 6. TP53INP2 induces non-shivering adaptive thermogenesis. Panels (**A**) to (**C**): control (LoxP) and KO^{Myf5} male mice at 3 months of age housed at 22°C and subjected to a chow diet (n=7 LoxP or KO^{Myf5} mice). (**A**) Energy expenditure, (**B**) oxygen consumption (VO_2) and (**C**) carbon dioxide production (VCO_2) plotted against body weight. (**D**) Oxygen consumption increase (ΔVO_2) upon norepinephrine injection (NE) and (**E**) area under the curve quantification in anesthetized mice at 30°C. LoxP or KO^{Myf5} mice were acclimated to the indicated temperatures for 2 months before performing the experiment (n=7–11 LoxP or KO^{Myf5} mice at 22ºC and n=5–9 LoxP or KO^{Myf5} mice at 30ºC). (**F**) High-resolution respirometry in iBAT isolated mitochondria (n=5–6 LoxP or KO^{Myf5} mice). Panels (**G**) to (**L**): LoxP and KO^{Myf5} male or female mice at 6 months of age housed at 22°C and subjected to a chow diet (n=4–9 LoxP or KO^{Myf5} mice). (**G**) Body weight. (**H**) Weight of iBAT. (**I**) Body weight gain and (**J**) fat mass gain from 3 to 6 months of age. (**K**) iBAT sections stained with DAPI (blue), wheat germ agglutinin

(WGA, green) and UCP1 (red). (**L**) UCP1 protein abundance in iBAT. Data are mean ± SEM. *p<0.05 vs. control group. Scale bar: 50 μm.

Figure 7. BAT-specific diet induced thermogenesis is impaired by *tp53inp2* ablation. Panels (**A**) to (**I**): control (LoxP) and KO^{Myf5} male mice at 6 months of age housed at 30°C for 5 months and subjected to a chow diet (CD) (n=8–12 LoxP or KO^{Myf5} mice) or to a high-fat diet (HFD) (n=8–10 LoxP or KO^{Myf5} mice). (**A**) Body weight. (**B**) Total fat mass. (**C**) Weight of iBAT. (**D**) Weight of ingWAT. (**E**) Weight of pgWAT. (**F**) Total lean mass. (**G**) Hematoxylin-eosin staining of iBAT sections, (**H**) lipid droplet (LD) number and (**I**) LD average area measurements. (**J**) Oxygen consumption increase (ΔVO_2) upon norepinephrine injection (NE) and (**K**) area under the curve quantification in anesthetized mice at 30°C. LoxP or KO^{Myf5} mice were acclimated to 30°C and to the indicated diet for 2 months before performing the experiment (n=5–9 LoxP or KO^{Myf5} mice subjected to a CD and n=7–9 LoxP or KO^{Myf5} mice subjected to a HFD). Data are mean ± SEM. *p<0.05 vs. LoxP control group. Scale bar: 100 μm.

Figure 8. TP53INP2 expression in brown adipose tissue is modulated by thermogenesis. (**A**) *Tp53inp2*, *Ucp1*, *Ppargc1a* and *Prdm16* mRNA levels (n=4–6), (**B**) TP53INP2 and UCP1 protein abundance and (**C**) quantification (n=5–6) in iBAT from control mice subjected to a chow diet (CD) or a high-fat diet (HFD) for 16 weeks. Panels (**D**) to (**G**): control (LoxP) and KO^{Myf5} male mice housed at 22°C and subjected to a HFD for a total of 16 weeks (n=6–10 LoxP or KO^{Myf5} mice). (**D**) Body weight. (**E**) Body weight gain. (**F**) Total fat mass. (**G**) Fat mass gain from 8 to 16 weeks of HFD. (**H**) *Tp53inp2*, *Ucp1*, *Ppargc1a* and *Prdm16* mRNA levels in iBAT from control mice housed at 22°C or 4°C

for 10 h (n=4–5). (**I**) *Tp53inp2*, *Ucp1*, *Ppargc1a* and *Prdm16* mRNA levels in iBAT from control mice housed at 22°C or at 30ºC for 5 months (n=5–6). (**J**) TP53INP2 protein abundance in human PAZ6 preadipocytes (Pre) or differentiated adipocytes (Ad) (n=3). (**K**) *Tp53inp2*, *Ucp1*, *Ppargc1a* and *Prdm16* mRNA levels in mature human PAZ6 brown adipocytes treated with vehicle (PBS), with 8-bromo-cAMP (8Br), with forskolin (FSK) or with dibutyryl-cAMP (dcAMP) for 4 h (n=3). (**L**) TP53INP2 protein abundance in mature human PAZ6 brown adipocytes treated with PBS, 8Br or FSK for 4 h (n=3). Data are mean ± SEM. *$p<0.05$ vs. control group in each case.

SUPPLEMENTARY DATA

Autophagy-mediated NCOR1 degradation is required for brown fat maturation and thermogenesis

Alba Sabaté-Pérez[1,2,3], Montserrat Romero[1,2,3], Paula Sànchez-Fernàndez-de-Landa[1,2,3], Stefania Carobbio[4,5], Michail Mouratidis[1], David Sala[1,2,3], Pablo Engel[6], Josep A Villena [3,7], Sam Virtue[4], Antonio Vidal-Puig[4,8], Manuel Palacín[1,2,9], Xavier Testar[2,3], and Antonio Zorzano[1,2,3]*

[1]Institute for Research in Biomedicine (IRB Barcelona). The Barcelona Institute of Science and Technology, Barcelona, Spain.

[2]Departament de Bioquímica i Biomedicina Molecular, Facultat de Biologia, Universitat de Barcelona, 08028 Barcelona, Spain.

[3]CIBER de Diabetes y Enfermedades Metabólicas Asociadas (CIBERDEM), Instituto de Salud Carlos III, Spain.

[4]Metabolic Research Laboratories, Institute of Metabolic Science, Addenbrooke's Hospital, University of Cambridge, Cambridge, CB2 0QQ, UK.

[5]Centro de Investigacion Principe Felipe, Valencia, Spain.

[6]Immunology Unit, Department of Biomedical Sciences, Faculty of Medicine and Health Sciences, Universitat de Barcelona, Spain.

[7]Laboratory of Metabolism and Obesity, Vall d'Hebron-Institut de Recerca, Universitat Autònoma de Barcelona, 08035 Barcelona, Spain.

[8]Wellcome Trust Sanger Institute, Wellcome Trust Genome Campus, Hinxton, Cambridge, CB10 1SA, UK.

[9]CIBER de Enfermedades Raras (CIBERER), Instituto de Salud Carlos III, Spain.

*Corresponding author. Institute for Research in Biomedicine, C/ Baldiri Reixac 10, 08028 Barcelona. Tel:+34-934037197; Fax:+34-934034717; E-mail: antonio.zorzano@irbbarcelona.org

Table S1. List of primers used for qPCR.

Gene name	Forward primer	Reverse primer
Arpc	AAGCGCGTCCTGGCATTGTCT	CCGCAGGGGCAGCAGTGGT
Cebpb	GGCCAAGAAGACGGTGGAC	GTCAGCTCCAGCACCTTGTG
Cox7a1	CAGCGTCATGGTCAGTCTGT	AGAAAACCGTGTGGCAGAG
Cox8b	GAACCATGAAGCCAACGACT	GCGAAGTTCACAGTGGTTCC
Dio2	CAGTGTGGTGCACGTCTCCAATC	TGAACCAAAGTTGACCACCAG
Tp53inp2	AACCACAGCCTGCTTCTAATACCTT	TCAGCCAGTCTCAACACAAAACAC
Elovl3	GCCTCTCATCCTCTGGTCCT	TGCCATAAACTTCCACATCCT
Ppargc1a	AGCCGTGACCACTGACAAC	GCTGCATGGTTCTGAGTGC
Pparg1	GGACTGTGTGACAGACAAGATTTGA	CTGAATATCAGTGGTTCACCGC
Pparg2	CTCTGTTTTATGCTGTTATGGGTGA	GGTCAACAGGAGAATCTCCCAG
Prdm16	CAGCACGGTGAAGCCATTC	GCGTGCATCCGCTTGTG
Dlk1	CTGTGTCAATGGAGTCTGCAAG	CTACGATCTCACAGAAGTTGC
Ucp1	GGAAAGGGACGACCCCTAATC	CCGGCAACAAGAGCTGACA
Ncor1	TGCGTCAGCTTTCTGTGATTCCACC	TGATTTCTGCCTCTGCGTTTTCCAT
Map1lc3b	AGCTCTTTGTTGGTGTGTAACTGTCT	TTGTCCTCACAGCTGACATGTATG
TP53INP2	CCTCCCCTTCTCCTCCAGTAAA	AGCCCAAAATTCAGTCTCACCA
UCP1	CTCACCGCAGGGAAAGAA	GGTTGCCCAATGAATACTGC
PPARGC1A	TGCATGAGTGTGTGCTCTGT	CAGCACACTCGATGTCACTC
PRDM16	TGGCTGCTTCTGGACTCA	ATATTATTTACAACGTCACCGTCACT
GAPDH	AGCCACATCGCTCAGACAC	GCCCAATACGACCAAATCC
ACTB	CACCAACTGGGACGACAT	ACAGCCTGGATAGCAACG
HPRT	CATTATGCTGAGGATTTGGAAAGG	CTTGAGCACACAGAGGGCTACA
TBP	TGTATCCACAGTGAATCTTGGTTG.	GGTTCGTGGCTCTCTTATCCTC

Figure S1

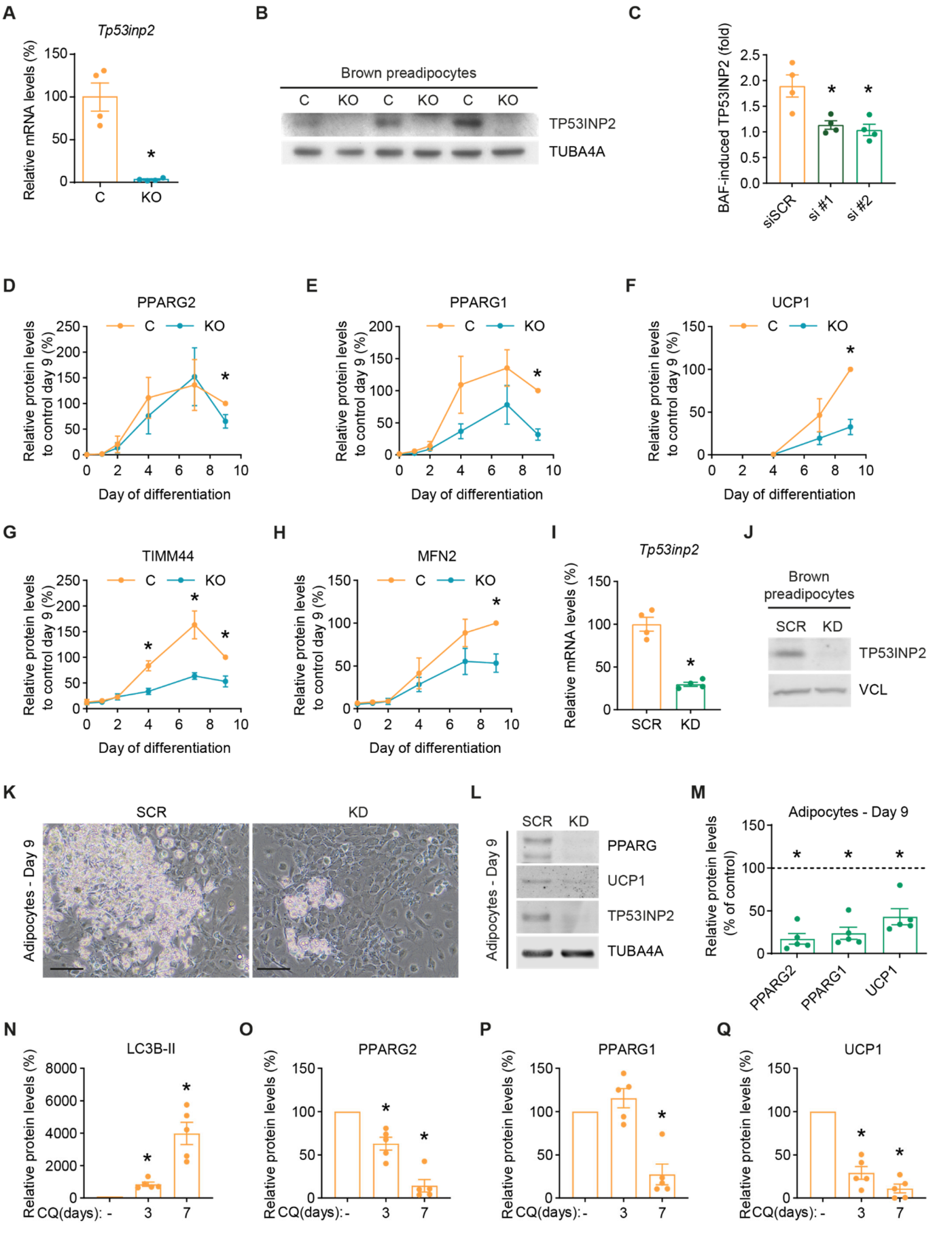
A
Tp53inp2
Relative mRNA levels (%)
150
100
50
0
C
KO
B
Brown preadipocytes
C KO C KO C KO
TP53INP2
TUBA4A
C
BAF-induced TP53INP2 (fold)
2.5
2.0
1.5
1.0
0.5
0.0
siSCR
si #1
si #2
D
PPARG2
C KO
Relative protein levels to control day 9 (%)
Day of differentiation
E
PPARG1
C KO
Relative protein levels to control day 9 (%)
Day of differentiation
F
UCP1
C KO
Relative protein levels to control day 9 (%)
Day of differentiation
G
TIMM44
C KO
Relative protein levels to control day 9 (%)
Day of differentiation
H
MFN2
C KO
Relative protein levels to control day 9 (%)
Day of differentiation
I
Tp53inp2
Relative mRNA levels (%)
SCR
KD
J
Brown preadipocytes
SCR KD
TP53INP2
VCL
K
SCR
KD
Adipocytes - Day 9
L
SCR KD
Adipocytes - Day 9
PPARG
UCP1
TP53INP2
TUBA4A
M
Adipocytes - Day 9
Relative protein levels (% of control)
PPARG2
PPARG1
UCP1
N
LC3B-II
Relative protein levels (%)
CQ(days): - 3 7
O
PPARG2
Relative protein levels (%)
CQ(days): - 3 7
P
PPARG1
Relative protein levels (%)
CQ(days): - 3 7
Q
UCP1
Relative protein levels (%)
CQ(days): - 3 7

Figure S1. TP53INP2 is a positive regulator of brown adipogenesis. (**A**) *Tp53inp2* mRNA levels (n=4) and (**B**) TP53INP2 protein abundance (n=3) in control (C) or *tp53inp2* knockout (KO) brown preadipocytes. (**C**) TP53INP2 fold accumulation in mouse brown preadipocytes transfected with siRNA control (siSCR) or with different siRNAs targeting *Tp53inp2* (si#1 and si#2) treated with vehicle or with 200 nM bafilomycin A_1 (BAF) for 4 h (n=4). (**D**) PPARG2, (**E**) PPARG1, (**F**) UCP1, (**G**) TIMM44 and (**H**) MFN2 protein quantification during differentiation of C or KO brown preadipocytes (n=3–6). Panels (**I**) to (**M**): control (SCR) or *tp53inp2* knockdown (KD) brown preadipocytes. (**I**) *Tp53inp2* mRNA levels (n=4). (**J**) TP53INP2 protein abundance (n=8). (**K**) Optical microscopy images at day 9 of differentiation. (**L**) PPARG, UCP1 and TP53INP2 protein abundance and (**M**) quantification at day 9 of differentiation (n=5). (**N**) LC3B-II, (**O**) PPARG2, (**P**) PPARG1 and (**Q**) UCP1 quantification in adipocytes treated for the last 3 or 7 days of differentiation with 15 μM chloroquine (CQ). Data are mean ± SEM. *$p<0.05$ vs. control group. Scale bar: 100 μm.

Figure S2

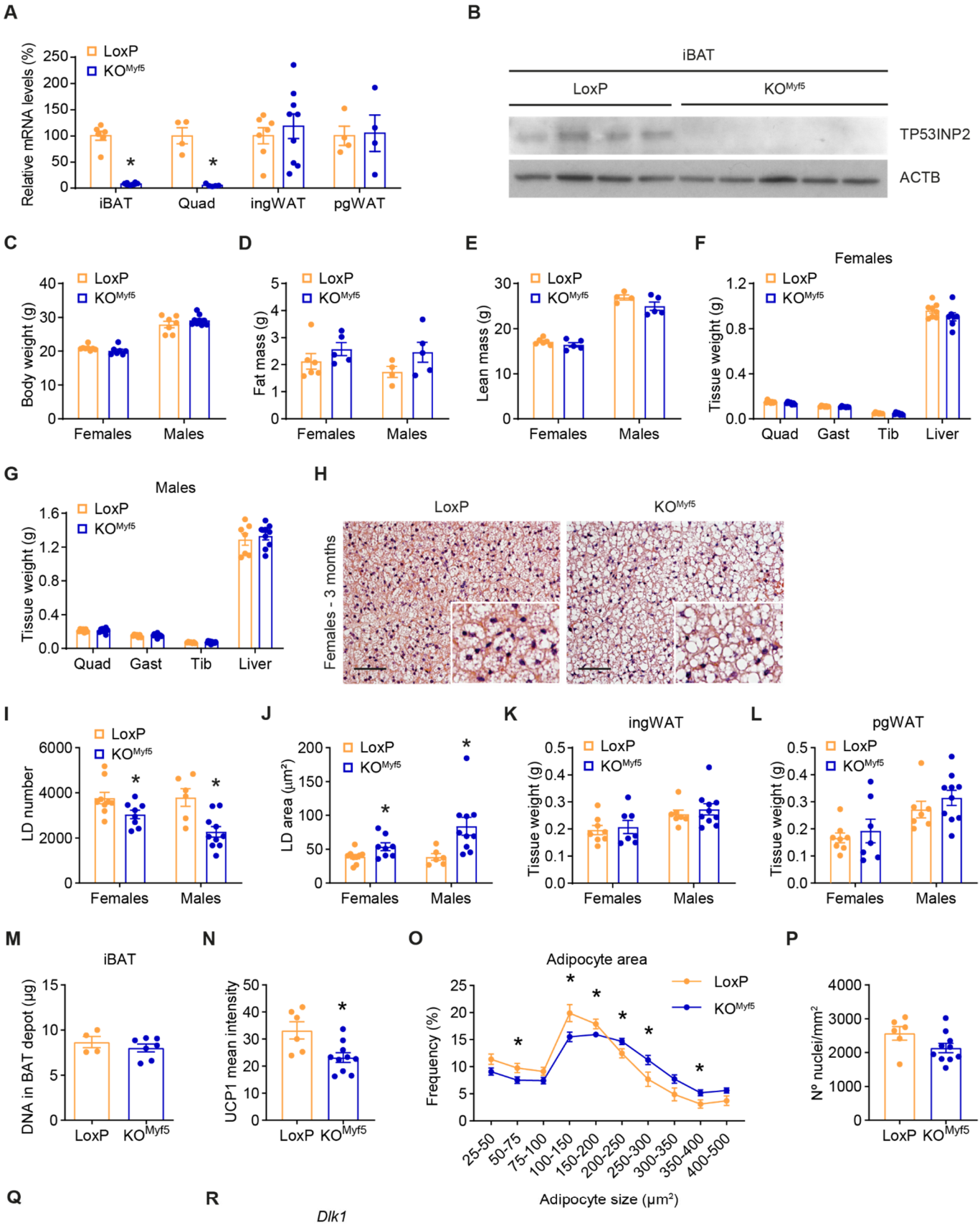
A
Relative mRNA levels (%)
LoxP
KOMyf5
iBAT
Quad
ingWAT
pgWAT
B
iBAT
LoxP
KOMyf5
TP53INP2
ACTB
C
Body weight (g)
Females
Males
D
Fat mass (g)
E
Lean mass (g)
F
Females
Tissue weight (g)
Quad
Gast
Tib
Liver
G
Males
H
LoxP
KOMyf5
Females - 3 months
I
LD number
J
LD area (µm²)
K
ingWAT
L
pgWAT
M
iBAT
DNA in BAT depot (µg)
N
UCP1 mean intensity
O
Adipocyte area
Frequency (%)
Adipocyte size (µm²)
25-50
50-75
75-100
100-150
150-200
200-250
250-300
300-350
350-400
400-500
P
Nº nuclei/mm²
Q
Nº adipocytes/mm²
R
Dlk1

Figure S2. TP53INP2 loss of function alters BAT identity. Panels (**A**) to (**R**): control (LoxP) and KO^{Myf5} male or female mice at 3 months of age housed at 22°C and subjected to a chow diet (n=7–9 LoxP or KO^{Myf5} mice). (**A**) *Tp53inp2* mRNA levels in iBAT, quadriceps muscle (Quad), ingWAT and pgWAT. (**B**) TP53INP2 protein abundance in iBAT. (**C**) Body weight. (**D**) Total fat mass. (**E**) Total lean mass. Weight of Quad, gastrocnemius muscle (Gast), tibialis muscle (Tib) and liver in (**F**) female and (**G**) male mice. (**H**) Hematoxylin-eosin staining of iBAT sections, (**I**) lipid droplet (LD) number and (**J**) LD average area measurements. (**K**) Weight of ingWAT. (**L**) Weight of pgWAT. (**M**) Total DNA amount per BAT depot. (**N**) UCP1 mean intensity, (**O**) adipocyte size distribution, (**P**) number of nuclei per surface unit and (**Q**) number of adipocytes per surface unit measurements in iBAT sections. (**R**) *Dlk1* mRNA levels in iBAT. Data are mean ± SEM. *p<0.05 vs. LoxP control group. Scale bar: 100 μm.

Figure S3

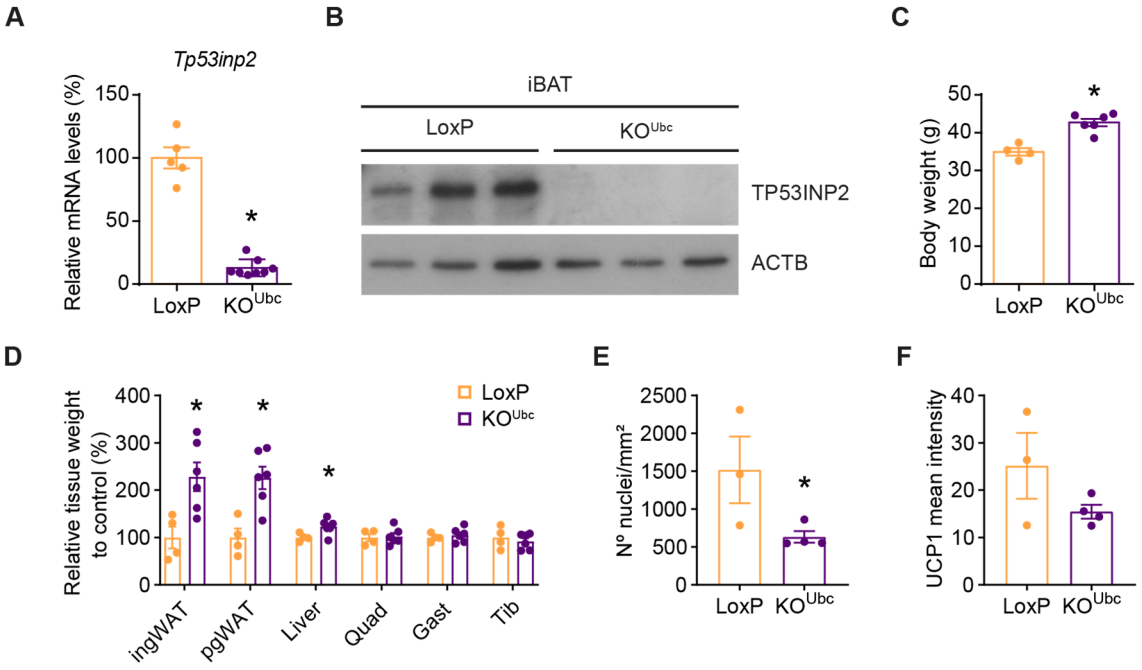
A
Tp53inp2
Relative mRNA levels (%)
150
100
50
0
*
LoxP
KOUbc
B
iBAT
LoxP
KOUbc
TP53INP2
ACTB
C
Body weight (g)
50
40
30
20
10
0
*
LoxP
KOUbc
D
Relative tissue weight to control (%)
400
300
200
100
0
LoxP
KOUbc
*
*
*
ingWAT
pgWAT
Liver
Quad
Gast
Tib
E
Nº nuclei/mm²
2500
2000
1500
1000
500
0
*
LoxP
KOUbc
F
UCP1 mean intensity
40
30
20
10
0
LoxP
KOUbc

Figure S3. Ablation of *tp53inp2* in adult mice enhances body weight and adiposity. Panels (**A**) to (**F**): Control (LoxP) and KO^{Ubc} male mice at 8 months of age housed at 22°C and subjected to a chow diet (n=4–8 LoxP or KO^{Ubc} mice). (**A**) *Tp53inp2* mRNA levels in iBAT. (**B**) T53INP2 protein abundance in iBAT. (**C**) Body weight. (**D**) Relative weight of ingWAT, pgWAT, liver, quadriceps (Quad), gastrocnemius (Gast) and tibialis muscles (Tib). (**E**) Number of nuclei per surface unit and (**F**) UCP1 mean intensity measurements in iBAT sections. Data are mean ± SEM. *$p<0.05$ vs. LoxP control group.

Figure S4

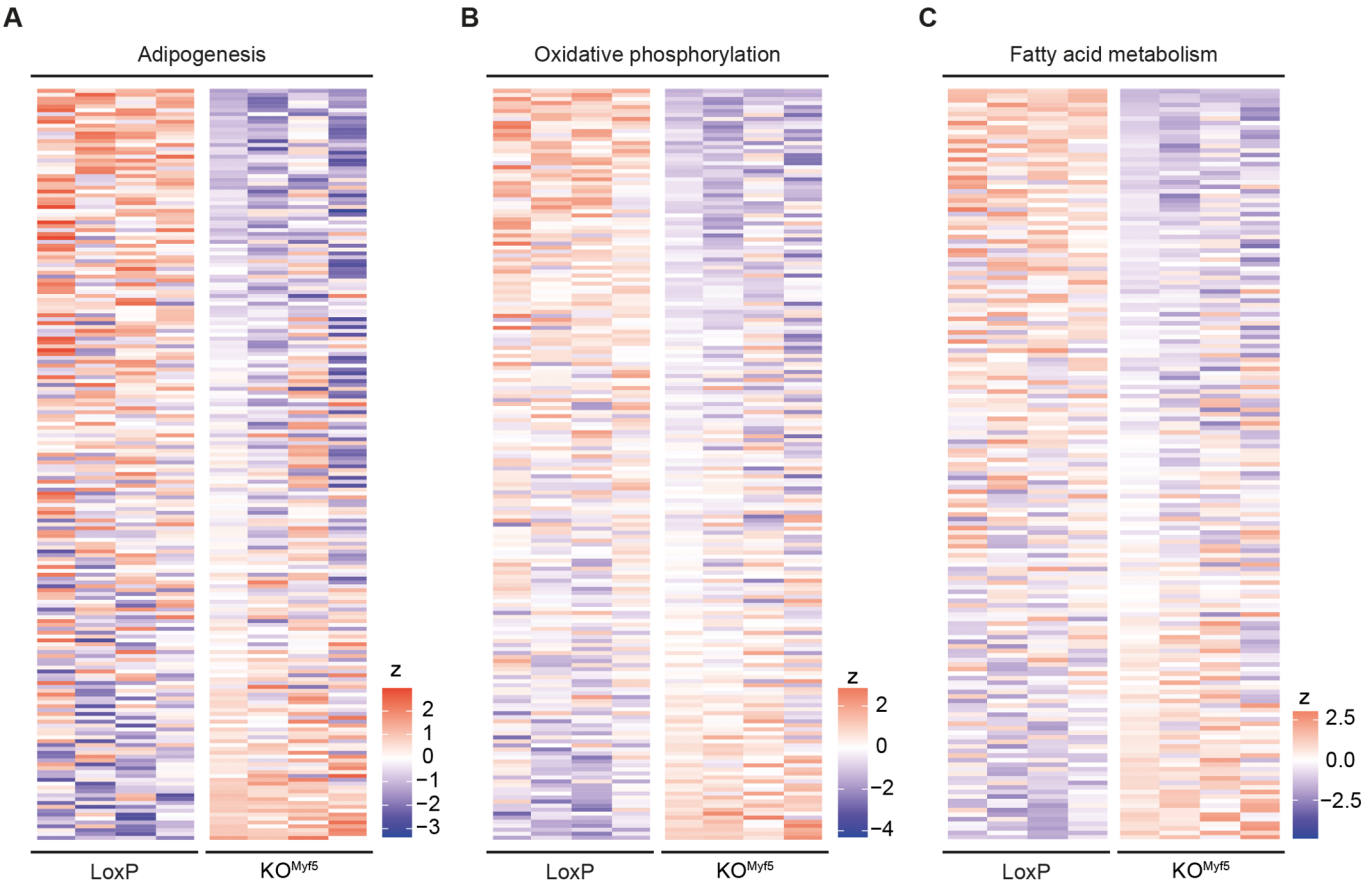
A
Adipogenesis
z
2
1
0
−1
−2
−3
LoxP
KOMyf5
B
Oxidative phosphorylation
z
2
0
−2
−4
LoxP
KOMyf5
C
Fatty acid metabolism
z
2.5
0.0
−2.5
LoxP
KOMyf5

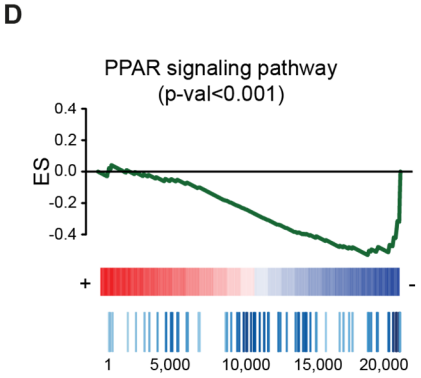
D
PPAR signaling pathway
(p-val<0.001)
ES
0.4
0.2
0.0
-0.2
-0.4
+
-
1
5,000
10,000
15,000
20,000

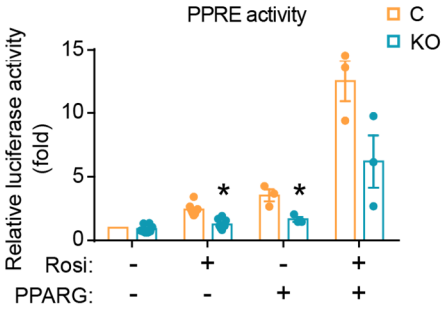
E
PPRE activity
C
KO
Relative luciferase activity
(fold)
15
10
5
0
*
*
Rosi:
PPARG:

Figure S4. TP53INP2 induces PPARG activity. Panels (**A**) to (**C**): transcriptomic analysis performed in iBAT from LoxP (n=4) or KO^{Myf5} mice (n=4). Heat maps showing gene expression modulation of (**A**) adipogenesis, (**B**) oxidative phosphorylation and (**C**) fatty acid metabolism gene sets from Broad Hallmarks. (**D**) Transcriptomic analysis performed in iBAT samples from LoxP (n=4) and KO^{Ubc} (n=4) mice. Enrichment plot (GSEA) of PPAR signaling pathway from Kyoto Encyclopedia of Genes and Genomes (KEGG) (p-val<0.001). (**E**) PPRE reporter activity in control (C) or *tp53inp2* knockout (KO) brown preadipocytes transfected with empty vector (-) or PPARG (+) and treated with vehicle (-) or with rosiglitazone (+) 1 μM for 24 h (n=3). Data are mean ± SEM. *p<0.05 vs. control group.

Figure S5

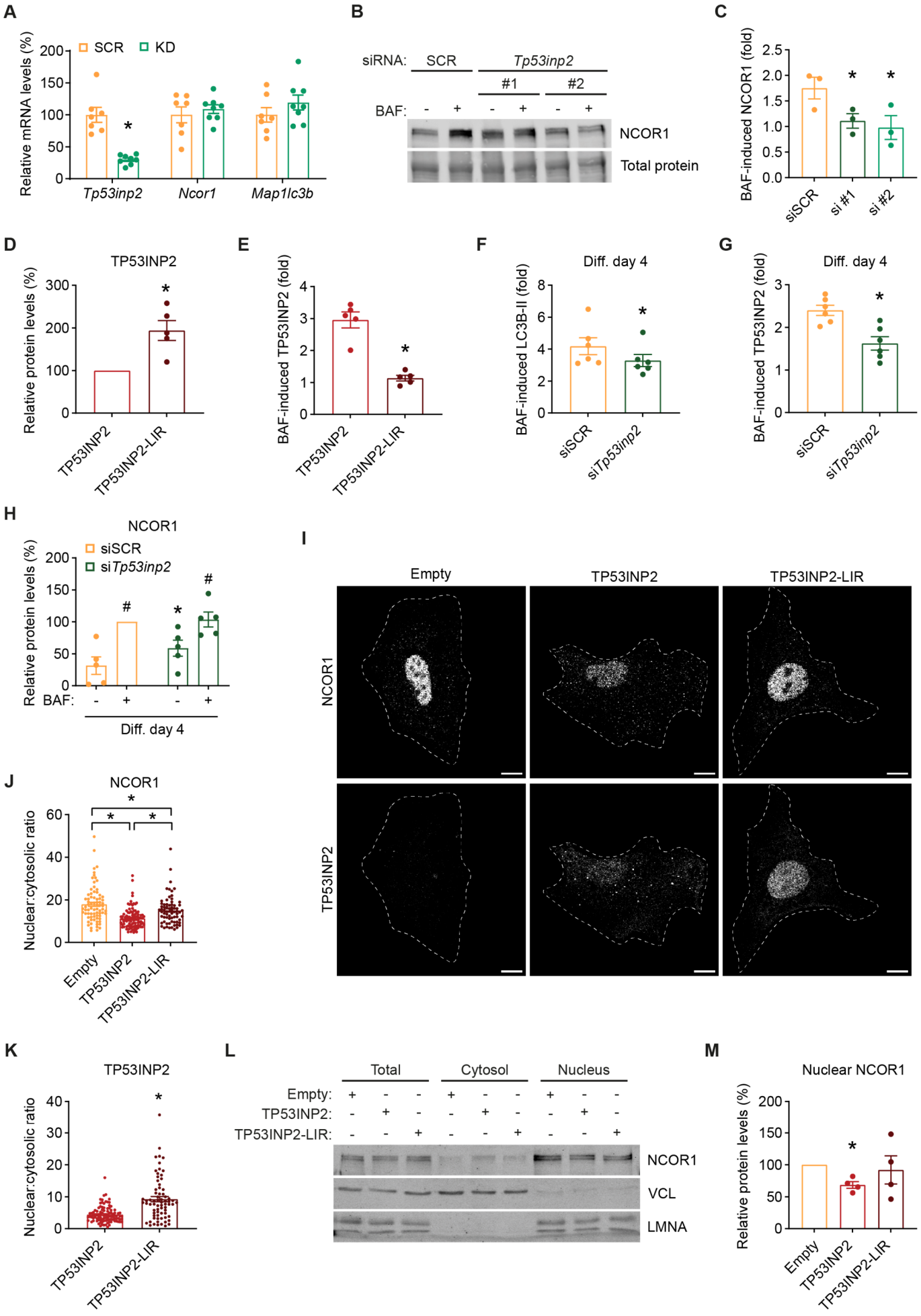
A
Relative mRNA levels (%)
SCR
KD
Tp53inp2
Ncor1
Map1lc3b
B
siRNA:
SCR
Tp53inp2
#1
#2
BAF:
NCOR1
Total protein
C
BAF-induced NCOR1 (fold)
siSCR
si#1
si#2
D
TP53INP2
Relative protein levels (%)
TP53INP2
TP53INP2-LIR
E
BAF-induced TP53INP2 (fold)
F
Diff. day 4
BAF-induced LC3B-II (fold)
siTp53inp2
G
BAF-induced TP53INP2 (fold)
H
NCOR1
siSCR
siTp53inp2
Diff. day 4
I
Empty
TP53INP2
TP53INP2-LIR
J
Nuclear:cytosolic ratio
K
L
Total
Cytosol
Nucleus
Empty:
TP53INP2:
TP53INP2-LIR:
VCL
LMNA
M
Nuclear NCOR1

Figure S5. TP53INP2 induces the autophagic degradation of the co-repressor NCOR1. (**A**) *Tp53inp2*, *Ncor1* and *Map1lc3b* mRNA levels in control (SCR) or *tp53inp2* knockdown (KD) brown preadipocytes (n=7–8). (**B**) NCOR1 protein abundance and (**C**) NCOR1 fold accumulation in mouse brown preadipocytes transfected with siRNA control (siSCR) or with different siRNAs targeting *Tp53inp2* (si#1 and si#2) and treated with vehicle (-) or with 200 nM bafilomycin A_1 (BAF) (+) for 4 h (n=3). (**D**) TP53INP2 protein abundance and (**E**) TP53INP2 fold accumulation in mouse brown preadipocytes stably overexpressing TP53INP2 or TP53INP2-LIR treated with vehicle (-) or with BAF (+) for 4 h (n=5). (**F**) LC3B-II and (**G**) TP53INP2 fold accumulation and (**H**) NCOR1 quantification in day 4 adipocytes transfected at day 2 with siRNA control (SCR) or against *Tp53inp2* in basal (-) or upon treatment with BAF (+) for the last 6 h (n=6, 6 and 5 respectively). Panels (**I**) to (**M**): control (Empty), TP53INP2 or TP53INP2-LIR stably overexpressing brown preadipocytes. (**I**) NCOR1 and TP53INP2 immunostaining, (**J**) NCOR1 and (**K**) TP53INP2 nuclear:cytosolic ratio quantification (representative experiment of n=3 independent experiments). (**L**) NCOR1 protein abundance in total, cytosolic and nuclear homogenates, and (**M**) nuclear NCOR1 quantification (n=4). Data are mean ± SEM. *p<0.05 vs. control group. #p<0.05 vs. non treated group. Scale bar: 10 μm.

Figure S6

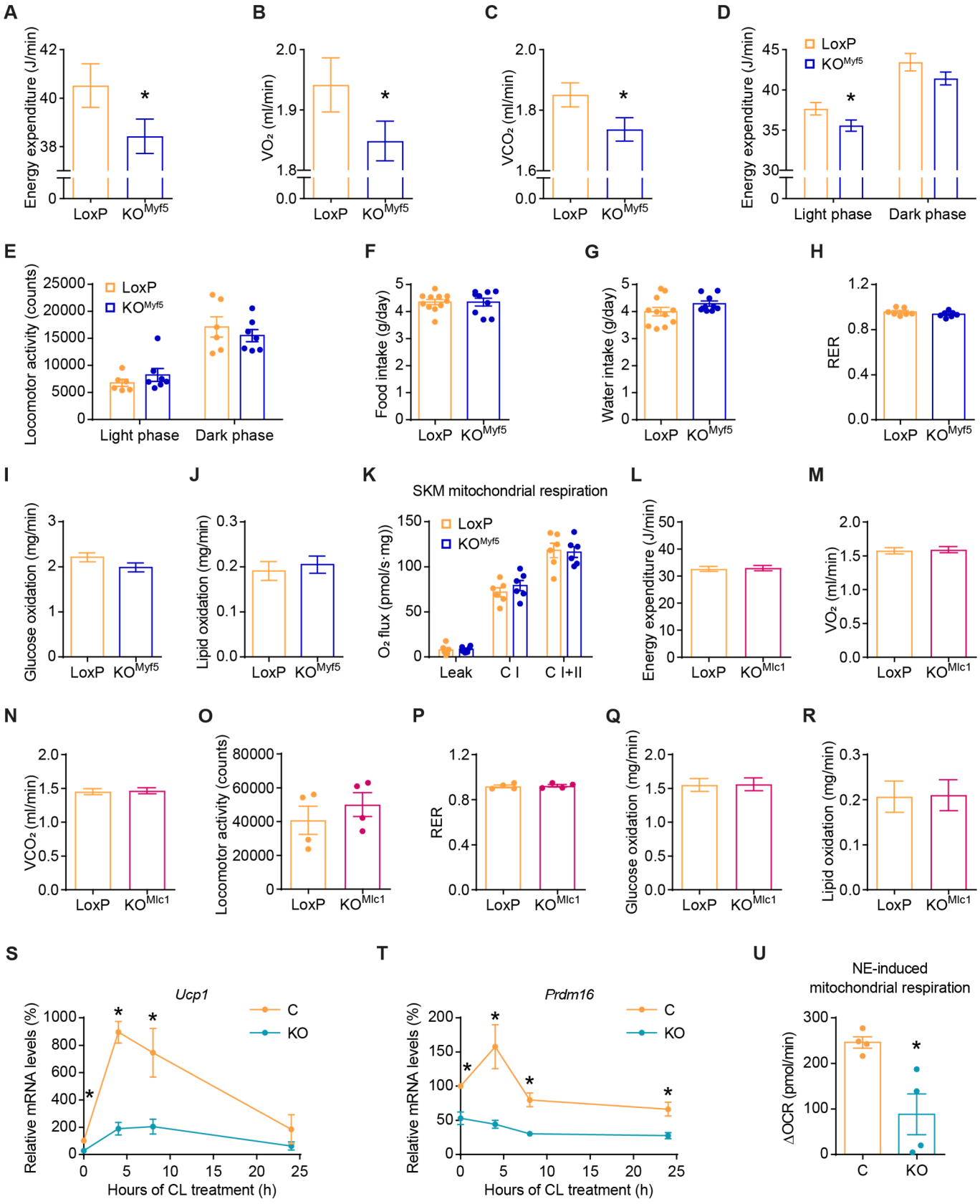
A
Energy expenditure (J/min)
LoxP
KO Myf5
B
VO₂ (ml/min)
C
VCO₂ (ml/min)
D
Energy expenditure (J/min)
Light phase
Dark phase
E
Locomotor activity (counts)
F
Food intake (g/day)
G
Water intake (g/day)
H
RER
I
Glucose oxidation (mg/min)
J
Lipid oxidation (mg/min)
K
SKM mitochondrial respiration
O₂ flux (pmol/s·mg))
Leak
C I
C I+II
L
Energy expenditure (J/min)
KO Mlc1
M
VO₂ (ml/min)
N
VCO₂ (ml/min)
O
Locomotor activity (counts)
P
RER
Q
Glucose oxidation (mg/min)
R
Lipid oxidation (mg/min)
S
Ucp1
C
KO
Relative mRNA levels (%)
Hours of CL treatment (h)
T
Prdm16
U
NE-induced
mitochondrial respiration
ΔOCR (pmol/min)

Figure S6. TP53INP2 enhances BAT specific thermogenesis. Panels (**A**) to (**K**): control (LoxP) and KO^{Myf5} male mice at 3 months of age housed at 22°C and subjected to a chow diet (n=7 LoxP or KO^{Myf5} mice). (**A**) Energy expenditure. (**B**) Oxygen consumption (VO_2). (**C**) Carbon dioxide production (VCO_2). (**D**) Energy expenditure during light (inactive) and dark (active) phase. (**E**) Locomotor activity during light and dark phase. (**F**) Food intake. (**G**) Water intake. (**H**) Respiratory exchange ratio (RER). (**I**) Glucose oxidation. (**J**) Lipid oxidation. (**K**) High-resolution respirometry in tibialis anterior muscle. Energy expenditure, VO_2, VCO_2, glucose oxidation and lipid oxidation are shown as adjusted means based on a normalized mouse weight of 29.4714 g determined using ANCOVA. Panels (**L**) to (**R**): control (LoxP) and KO^{Mlc1} male mice at 4 months of age housed at 22°C and subjected to a chow diet (n=4 LoxP or KO^{Mlc1} mice). (**L**) Energy expenditure. (**M**) VO_2. (**N**) VCO_2. (**O**) Locomotor activity. (**P**) RER. (**Q**) Glucose oxidation. (**R**) Lipid oxidation. Energy expenditure, VO_2, VCO_2, glucose oxidation and lipid oxidation are shown as adjusted means based on a normalized mouse weight of 27.0625 g determined using ANCOVA. Panels (**S**) to (**U**): control (C) and *tp53inp2* knockout (KO) mouse brown adipocytes. (**S**) *Ucp1* and (**T**) *Prdm16* mRNA levels in adipocytes treated with CL-316,243 (CL) for different times (n=4). (**U**) Norepinephrine (NE)-induced (1 μM) mitochondrial respiration (ΔOCR) (n=4). Data are mean ± SEM. *$p<0.05$ vs. control group.

Figure S7

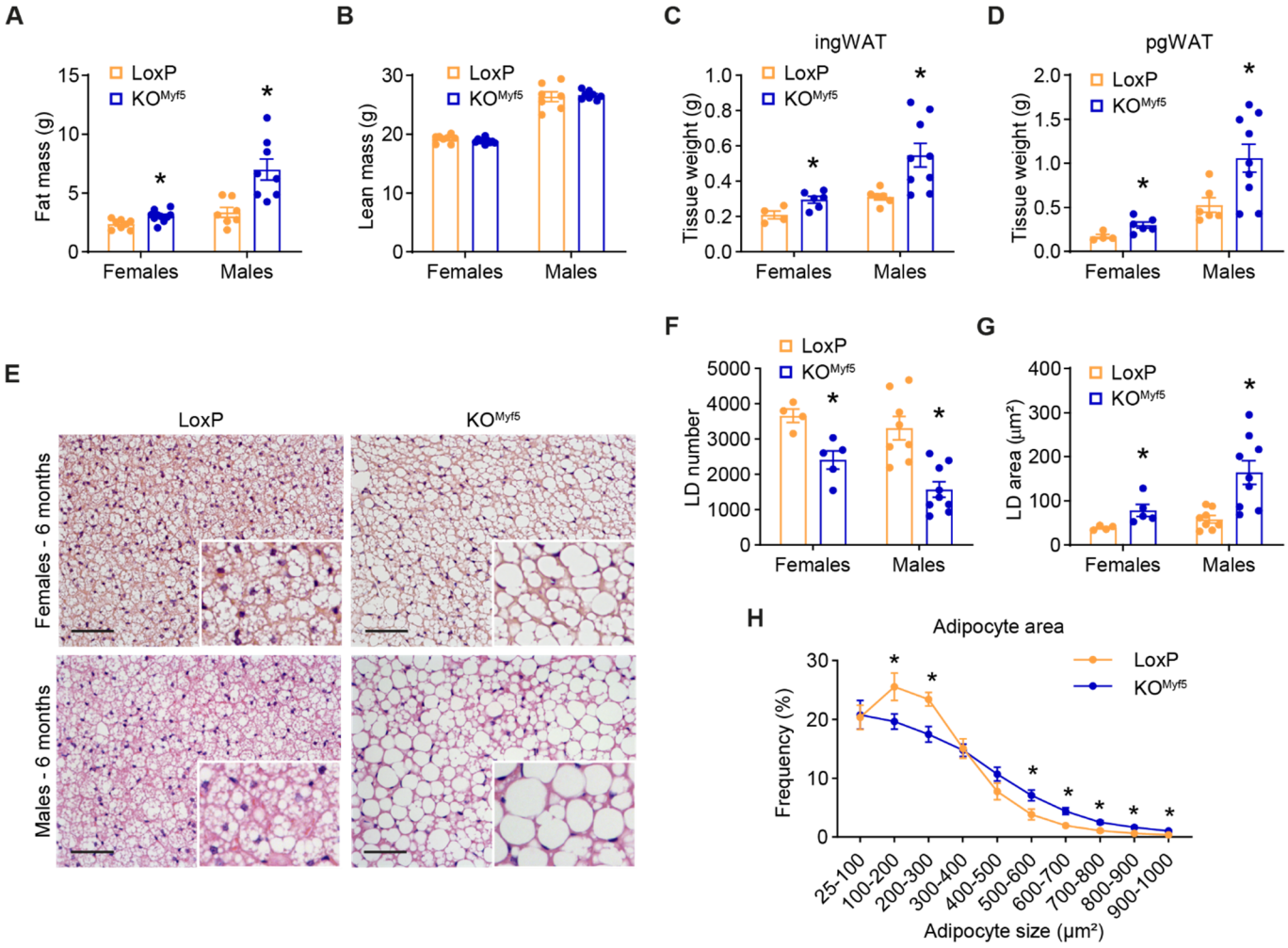
A
Fat mass (g)
LoxP
KOMyf5
Females
Males
B
Lean mass (g)
C
ingWAT
Tissue weight (g)
D
pgWAT
E
LoxP
KOMyf5
Females - 6 months
Males - 6 months
F
LD number
G
LD area (µm²)
H
Adipocyte area
Frequency (%)
Adipocyte size (µm²)
25-100
100-200
200-300
300-400
400-500
500-600
600-700
700-800
800-900
900-1000

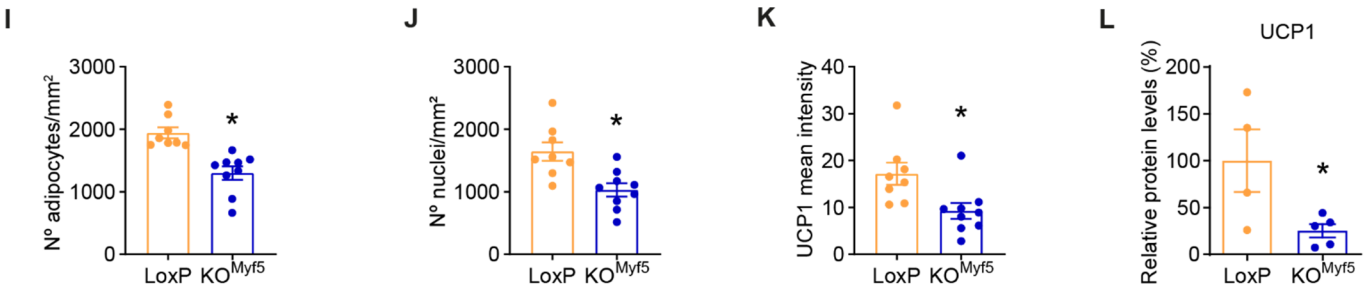
I
Nº adipocytes/mm²
J
Nº nuclei/mm²
K
UCP1 mean intensity
L
UCP1
Relative protein levels (%)
LoxP
KOMyf5

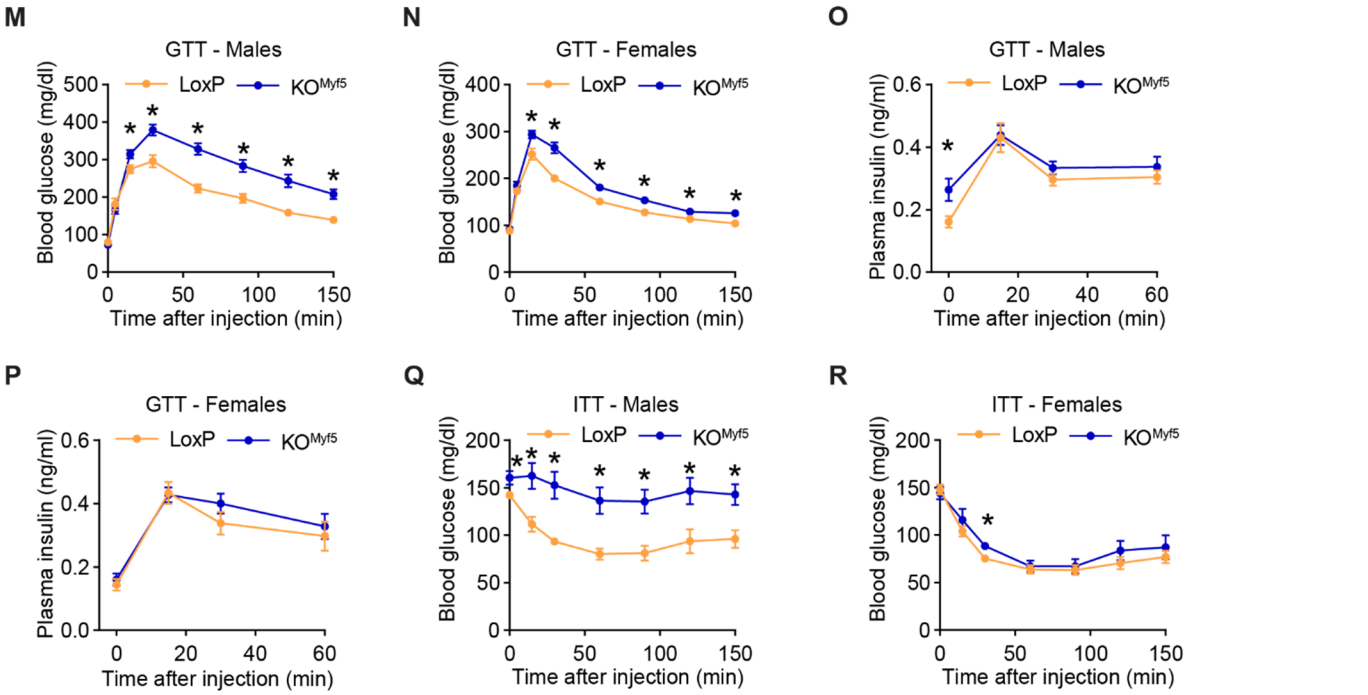
M
GTT - Males
Blood glucose (mg/dl)
Time after injection (min)
N
GTT - Females
O
Plasma insulin (ng/ml)
P
Q
ITT - Males
R
ITT - Females

Figure S7. TP53INP2 prevents fat mass expansion through BAT thermogenesis. Panels (**A**) to (**L**): control (LoxP) and KO^{Myf5} male or female mice at 6 months of age housed at 22°C and subjected to a chow diet (n=4–9 LoxP or KO^{Myf5} mice). (**A**) Total fat mass. (**B**) Total lean mass. (**C**) Weight of ingWAT. (**D**) Weight of pgWAT. (**E**) Hematoxylin-eosin staining of iBAT sections, (**F**) lipid droplet (LD) number and (**G**) LD average area measurements. (**H**) Adipocyte size distribution, (**I**) number of adipocytes per surface unit, (**J**) number of nuclei per surface unit and (**K**) UCP1 mean intensity measurements in iBAT sections. (**L**) UCP1 protein quantification in iBAT. Panels (**M**) to (**R**): LoxP and KO^{Myf5} male or female mice at 3 months of age housed at 22°C and subjected to a chow diet (n=7–10 LoxP or KO^{Myf5} mice). Blood glucose levels during glucose tolerance test (GTT, 2 g/kg) in (**M**) males or (**N**) females. Plasma insulin levels during GTT in (**O**) males or (**P**) females. Blood glucose levels during insulin tolerance test (ITT, 0.7 U/kg) in (**Q**) males or (**R**) females. Data are mean ± SEM. *$p<0.05$ vs. LoxP control group. Scale bar: 100 µm.

Figure S8

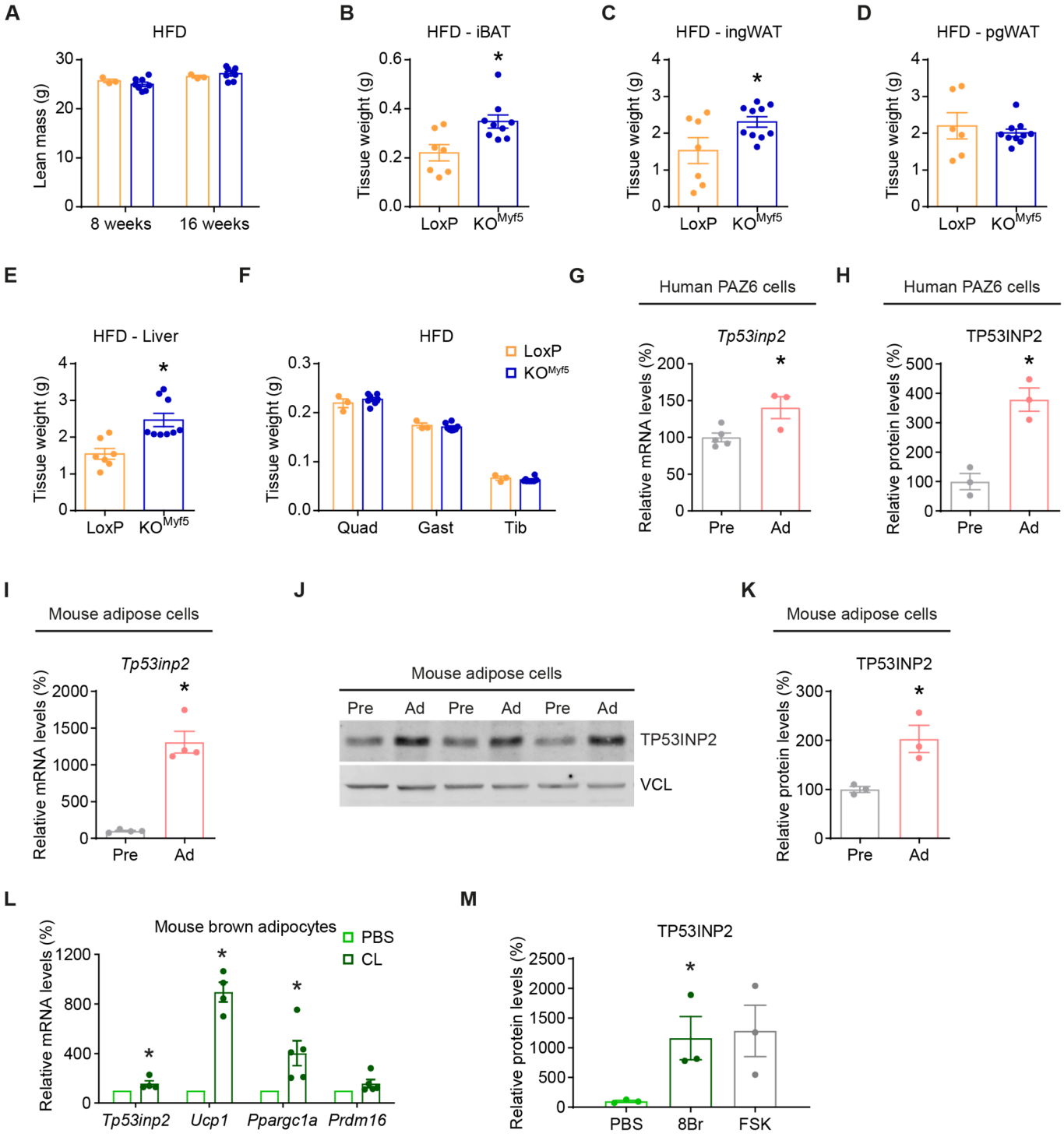
A
HFD
Lean mass (g)
8 weeks
16 weeks
B
HFD - iBAT
Tissue weight (g)
LoxP
KOMyf5
C
HFD - ingWAT
D
HFD - pgWAT
E
HFD - Liver
F
HFD
LoxP
KOMyf5
Quad
Gast
Tib
G
Human PAZ6 cells
Tp53inp2
Relative mRNA levels (%)
Pre
Ad
H
Human PAZ6 cells
TP53INP2
Relative protein levels (%)
I
Mouse adipose cells
Tp53inp2
J
Mouse adipose cells
Pre
Ad
TP53INP2
VCL
K
Mouse adipose cells
TP53INP2
L
Mouse brown adipocytes
PBS
CL
Tp53inp2
Ucp1
Ppargc1a
Prdm16
M
TP53INP2
PBS
8Br
FSK

Figure S8. Thermogenesis activity and TP53INP2 expression are modulated in parallel. Panels (**A**) to (**F**): control (LoxP) and KO^{Myf5} male mice housed at 22°C and subjected to a high-fat diet (HFD) for a total of 16 weeks (n=6–10 LoxP or KO^{Myf5} mice). (**A**) Total lean mass. (**B**) Weight of iBAT. (**C**) Weight of ingWAT. (**D**) Weight of pgWAT. (**E**) Weight of liver. (**F**) Weight of quadriceps (Quad), gastrocnemius (Gast) or tibialis (Tib) muscles. (**G**) *Tp53inp2* mRNA levels and (**H**) TP53INP2 protein quantification in human PAZ6 preadipocytes (Pre) or differentiated adipocytes (Ad) (n=3). (**I**) *Tp53inp2* mRNA levels (n=4), (**J**) TP53INP2 protein abundance and (**K**) quantification (n=3) in mouse brown preadipocytes (Pre) or differentiated brown adipocytes (Ad). (**L**) *Tp53inp2*, *Ucp1*, *Ppargc1a* and *Prdm16* mRNA levels in mature mouse brown adipocytes treated with vehicle (PBS) or with the β3-adrenergic agonist CL-316,243 (CL) for 4 h (n=4). (**M**) TP53INP2 protein quantification in mature human PAZ6 brown adipocytes treated with vehicle (PBS), with 8-bromo-cAMP (8Br) or with forskolin (FSK) for 4 h (n=3). Data are mean ± SEM. *$p<0.05$ vs. control group in each case.